

1 **Influence of topography and winds on the distribution of water masses on**
2 **the Antarctic Continental Shelf**

3 Christopher Y. S. Bull^a, David R. Munday^b, Adrian Jenkins^a

4 ^a *Department of Geography and Environmental Sciences, Northumbria University, Newcastle upon Tyne, UK.*

5 ^b *British Antarctic Survey, Cambridge, United Kingdom.*

6
7 *Corresponding author:* Christopher Y. S. Bull, christopher.bull@northumbria.ac.uk
8

Central to improving our understanding of ocean temperature change on Antarctica's continental shelf is a better understanding of how the ocean circulation drives the onshore flux of warm deep waters across the shelf break. This study uses a primitive equation ocean model to explore how the circulation regime and changes in surface stress influence the temperature structure on Antarctica's shelf seas. As the shelf temperature changes are largely driven by ocean circulation changes, understanding these becomes our focus. A simple barotropic model is used to describe the linear theory of the difference between throughflow and gyres regimes, and their expected response to changes in forcing. This theory informs our understanding of the barotropic circulation response of the primitive equation model where a momentum and heat budget confirm that over the simulated equilibrated timescales with surface forcing changes, the response is first-order linear. Consistent with previous findings, we find that climate change projection-like wind shifts (stronger westerlies that shift south) have a direct influence on Ekman processes across the shelf break and upwell warmer waters onto the shelf. We also find that the circulation regime (throughflow or gyre – determined by basin geometry), influences the mean shelf temperature and how susceptible the existing shelf temperatures are to changes in surface stress. While the throughflow regime can experience a complete transition in on-shelf temperatures when the transition between westerly and easterly winds shifts southward, we find relatively modest warming at the coast in a gyre regime. Combinations of these regimes also experience coastal warming under a constant positive offset in the winds.

SIGNIFICANCE STATEMENT

The Antarctic Slope Front determines how much warm water flows onto the shelf and the subsequent heat that is available to melt the ice shelves. This study explores the impact of basin geometry and wind shifts on the large-scale ocean circulation around Antarctica's continental shelf with a focus on understanding changes in shelf temperature near an imagined ice front. Here, meridional topographic barriers change geometry, shedding insight into how different water temperatures on the shelf coalesce despite having the same initial conditions and wind forcing. Wind perturbation simulations suggest why some regions are more sensitive to shifts in winds than others. These findings highlight an underappreciated yet fundamentally important topographical constraint under future changes in winds.

1 Introduction

The Southern Ocean (Figure 1a) circulation has mixtures of both throughflow and gyre regimes, where the wind and sea-ice stress determine the momentum input driving the ocean circulation (Figure 1b). Throughflow regime currents are the eastward flowing Antarctic Circumpolar Current (ACC) and a shelf confined westward flow that is effectively a combination of the Antarctic Slope Current (ASC) and the Antarctic Coastal Current. The ACC is predominantly driven by wind and buoyancy forcing and is the world's strongest current (Olbers et al., 2012); modern estimates of Drake Passage transport vary between 137 ± 7 Sv (thermal wind only; *Meredith et al.*, 2011) and 173.3 ± 10.7 Sv for total transport (Donohue et al., 2016). Several studies in realistic settings (e.g. *Masich et al.*, 2015) have confirmed that topographic form stress is the dominant sink of momentum in throughflow regions. Note that the ASC is not quite a circumpolar feature; it is not found along the western Antarctic peninsula where the ACC flows along the continental slope (Thompson et al., 2018; Whitworth et al., 1998). In between the ACC and ASC is the Antarctic Slope Front (ASF), a landward thickening of the layer of cold surface waters that, through its position on the continental shelf break, regulates onshore heat transport associated with inflow of warmer sub-surface waters (Thompson et al., 2018). Gyre regimes, form where f/h gradients are sufficiently steep to block throughflow (Olbers et al., 2007; Patmore et al., 2019; Wilson et al., 2022), and are characterized by the clockwise flowing Weddell, Ross and Australian-Antarctic gyres. The Weddell and Ross gyres with transports of 30-100 and 23 ± 8 Sv (respectively) are sensitive to local changes in wind stress curl (Armitage et al., 2018; Dotto et al., 2018; Gómez-Valdivia et al., 2023; Neme et al., 2021) and buoyancy forcing (Gray & Riser, 2014; Hogg & Gayen, 2020).

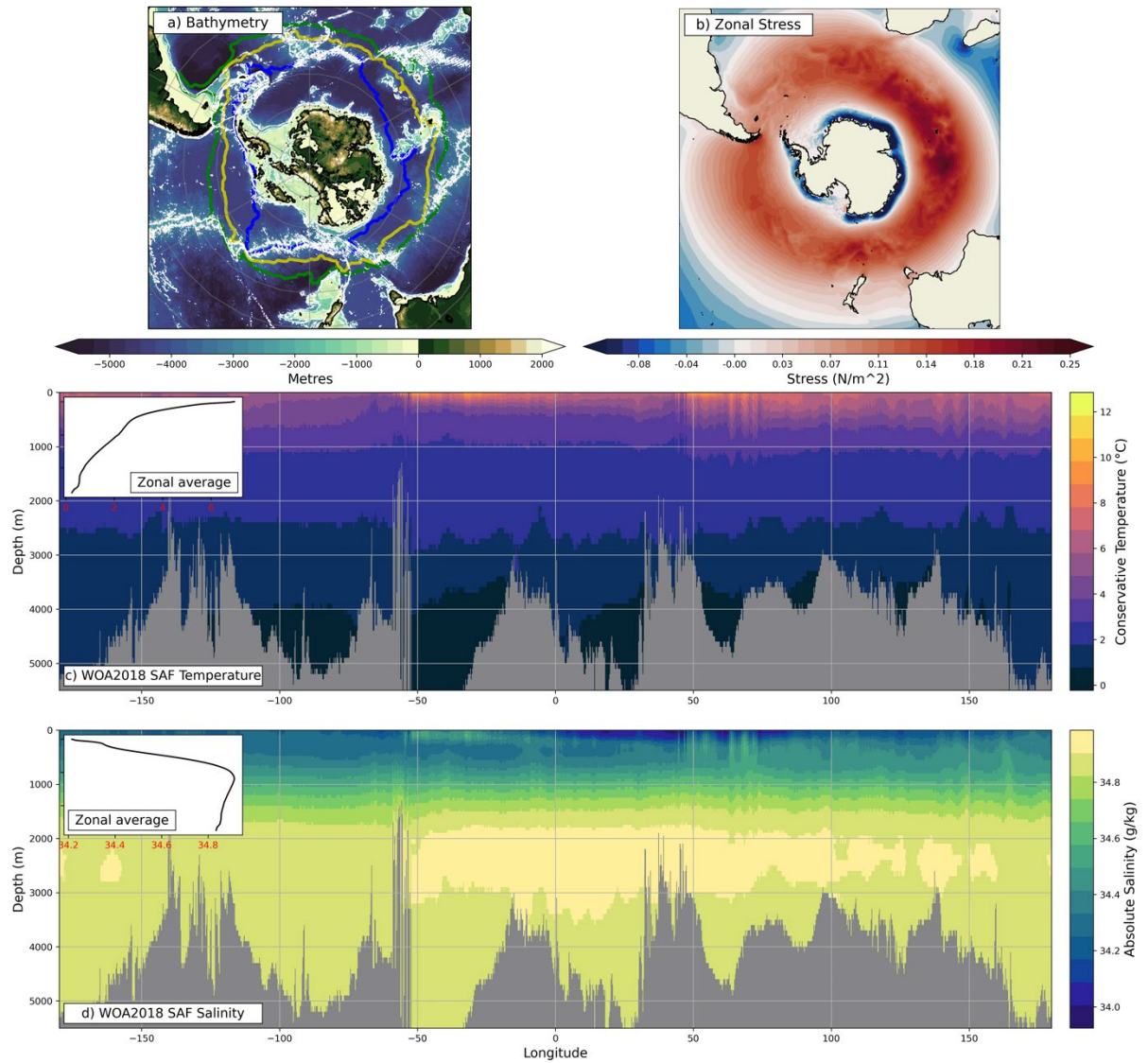


Figure 1. a) ETOPO1 bathymetry, thick contours indicate Southern Boundary (blue), Polar Front (yellow), and Subantarctic Front (green) from *Park et al.* (2019); thin white contours highlight -3000m, -2000m, -1000m isobaths, and black contour is 0m. b) JRA zonal surface stress (time-mean 1986-2000; both wind and sea ice), black contour is the surface land mask. WOA2018 Subantarctic Front (green contour in panel a); c) Temperature and d) Salinity. The insets in c-d show the zonal average of temperature and salinity, respectively; these T/S profiles are used as initial and northern boundary restoring conditions for the modelling configuration in this study (see Section 3b).

At the Antarctic coast, ice shelves flow from the ice sheet and are vulnerable to future changes in sub-surface ocean temperatures at the southern margins. In the case of the Weddell and Ross gyres, the related ice shelves experience low melt rates because warm water has limited direct access to the ice-shelf base (Pritchard et al., 2012). Much of the recent interest in the ASF (Thompson et al., 2018) is due to its capacity to modulate the inshore flux of Circumpolar Deep Water melting the ice shelves. The ASC is driven by the

79 along slope westward wind stress (Pauthenet et al., 2021; Thompson et al., 2018) and
80 buoyancy forcing (Hattermann, 2018). The winds over the Southern Ocean vary on several
81 timescales and all of the Southern Ocean current systems, are expected to show some
82 sensitivity to the projected southward shift in winds (e.g. Bracegirdle et al., 2013; Goyal et
83 al., 2021) although a signal has not necessarily been observed (e.g. Armitage et al., 2018;
84 Stewart, 2021).

85
86 Considerable work has gone into understanding the anticipated changes in Southern
87 Ocean circulation as a result of changes in the westerly winds, particularly the circumpolar
88 transport of the ACC (e.g. Farneti et al., 2015; Munday et al., 2013; Purich & England, 2021;
89 Spence et al., 2017). Eddy saturation is a regime in which the ACC's total transport becomes
90 insensitive to surface wind stress changes. Substantial work has gone into characterising eddy
91 saturation of the ACC and relating it to eddy processes (Gnanadesikan & Hallberg, 2000;
92 Straub, 1993; Tansley & Marshall, 2001). In an eddy saturated state, despite the total
93 transport not changing, we would expect the barotropic transport to respond to changes in
94 surface forcing (Constantinou & Hogg, 2019). Using a more realistic configuration, *Spence*
95 *et al.* (2014) has shown that anticipated southward shifts in the southern ocean winds lead to
96 a change in Ekman dynamics at the coast. Specifically, reduced Ekman pumping at the coast
97 leads to a flattening of isotherms, enabling increased inflow of warm waters onto the shelf.
98 Presently, there is a tendency to apply these arguments around all of Antarctica, however
99 some regions are more susceptible to these shifts than others (Verfaillie et al., 2022). Under a
100 uniform 4° southward shift, the Amundsen Sea warms the most, whereas the Ross Sea cools
101 and the Weddell Sea shelf modestly warms (Figure S5b in *Spence et al.* 2014). Meridionally
102 uniform changes to the winds would not be expected to change the horizontal circulation of a
103 gyre regime but would have a strong response in a throughflow regime (Olbers, 1998; Vallis,
104 2017; Veronis, 1996). The work to date has focused on southward wind shifts (stronger
105 westerlies) that assume a throughflow-like regime, this suggests that we might be over-
106 estimating the effect. A natural question arises: given the projected wind changes are similar
107 to a positive constant offset in the winds (westerly strengthening and southward shift), how
108 do we expect the Southern Ocean to respond in places where there are a mixture of
109 throughflow and gyre regimes? To begin work on this last question, we revise the seminal
110 linear theory of throughflow and gyre regimes.

In their canonical form, a circumpolar-like throughflow (e.g. Antarctic Circumpolar Current) and an ocean gyre (e.g. Weddell gyre) can be created in an open re-entrant channel with a uniform wind and a closed box with a half cosine wind, respectively (Vallis, 2017). In the re-entrant channel case (hereafter, “throughflow regime”), a uniform eastward wind drives an eastward current. Eddy saturation aside, increasing the strength of the wind uniformly, might be expected to drive a stronger eastward current. The closed box (hereafter, “gyre regime”) analogue might feel like a paradox in comparison; adding a uniform wind to the half cosine wind, does not strengthen the circulation (Hughes, 1997). This is because the circulation strength depends on the wind stress curl. Here, the curl is the meridional gradient of zonal velocity and thus a uniform change in wind does not change the horizontal circulation (Veronis, 1996). In a throughflow regime, e.g., a re-entrant channel with a flat bottom, a momentum budget reveals a primary balance between zonal momentum input from the wind balanced by bottom friction. The flat bottom results in an unrealistically strong ACC and a large sea surface height (SSH) gradient (Hidaka & Tsuchiya, 1953; Munday et al., 2015; Olbers et al., 2007). *Munk and Palmen* (1951) showed that in the presence of significant bathymetry, topographic form stress (as it is now known) is a more effective sink of momentum, slowing down the eastward flow and creating a meridional geostrophic flow that is confined to below the height of the bathymetry. In contrast, in the closed box, the insightful perspective (Hughes, 1997; Olbers, 1998; Styles et al., 2021) is taken via the curl of the momentum equation. For this system, a vorticity budget reveals a primary balance between the curl of the wind stress acting as a source of vorticity and the curl of the bottom friction (flat bottomed) or the curl of the topographic form stress (significant bathymetry) acting as a vorticity sink. This profound importance of boundary conditions has led to the tendency to focus on these distinct dynamical balances when studying throughflows as compared to gyres (Olbers et al., 2012; Vallis, 2017). As the real system exhibits both kinds of flows, we need a better understanding of the transitory dynamics of these two regimes so we can better predict how they will change as their forcing evolves with climate change.

The goal of this study then is to re-visit channel and gyre regimes in the context of an idealised Southern Ocean configuration with southward (uniform offset) wind shift experiments. The community, for the purpose of attribution, needs to understand the

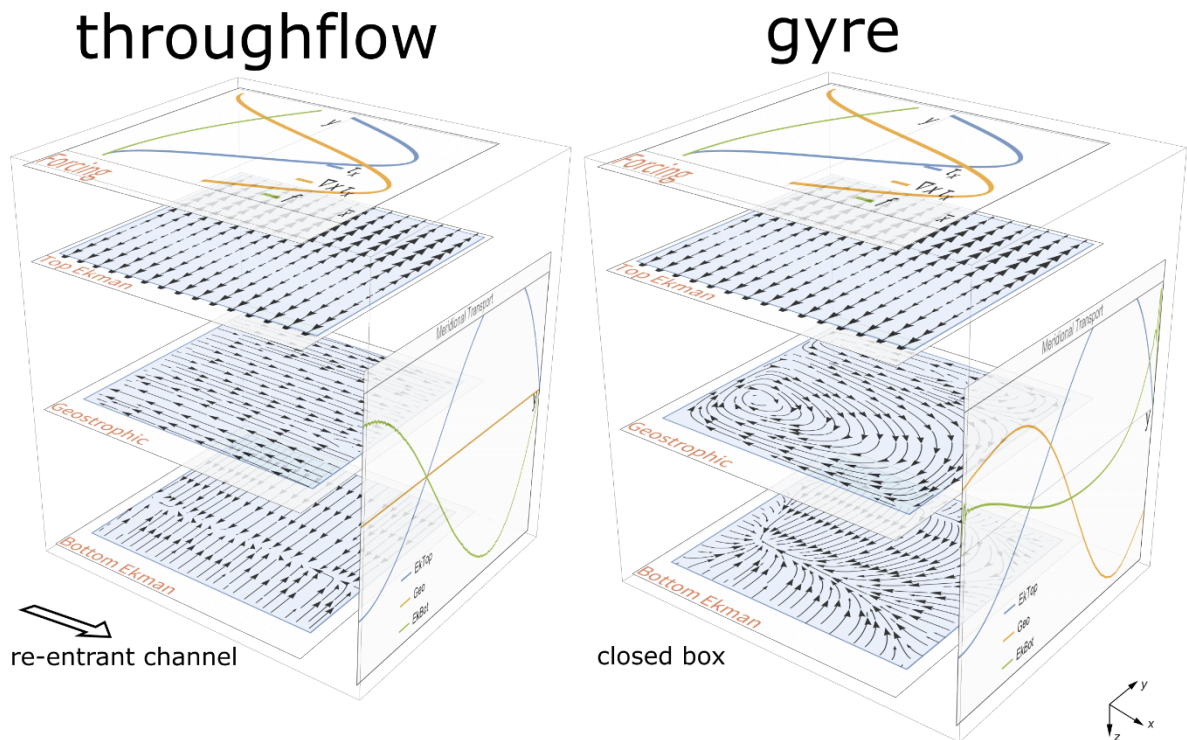
implications of a change in wind strength, shifts and curl change; using uniform offsets makes progress towards disentangling these issues. We will use barotropic linear theory to understand better the differing response to a uniform change in surface stress in a throughflow versus a gyre regime. We then investigate with a primitive equation ocean model, how the system is complicated by the inclusion of a continental shelf, mixtures of flow regimes and baroclinicity. Whilst the integrated changes in horizontal circulation from a re-entrant channel to a hard wall are well known (e.g. Olbers, 1998; Tansley & Marshall, 2001; Vallis, 2017), we believe this is the first time an incremental mixture of these two regimes has been studied in terms of wind shifts and the temperature structure on the shelf. Two questions arise:

1. Subject to the same starting point, how are the mean shelf temperatures influenced by a hierarchy of basin geometries?

2. How is basin geometry important for modulating shelf temperature changes with shifts in the winds?

The paper is presented as follows. Section 2 has a synthesis of existing linear theory as related to throughflow and gyre regimes in the Southern Ocean where changes in forcing are also considered. The remainder of the paper builds on this understanding, using the primitive equation model NEMO, adding complexity through: a continental shelf, deep ocean ridge and walls that create combinations of throughflow and gyre regimes. The numerical model description, experiment design and results are in Sections 3a, 3b, 4, respectively. A summary and discussion is given in Section 5.

166 2 Southern Ocean circulation theory: throughflow versus gyre regimes



167
 168 Figure 2. Comparison of throughflow (left) and gyre (right) regimes for an idealized Southern Ocean wind
 169 stress in a single-layer ocean. The channel has a re-entrant east-west boundary whereas the gyre has walls
 170 on all sides. Horizontal layers show the forcing, Ekman and Geostrophic layers. The “forcing” layer shows
 171 the zonally averaged wind stress, wind stress curl and Coriolis parameter. The circulation layers are: top
 172 Ekman, geostrophic and bottom Ekman transports, respectively; the barotropic streamfunction is the sum
 173 of the three layers (see Figure 3). The vertical panel shows the zonally averaged meridional transport for
 174 each component.

175 Figure 2 utilises the *Stommel* (1948) planetary geostrophic equations to highlight
 176 throughflow and gyre circulations within an idealised, barotropic, flat-bottom configuration
 177 and rigid lid. The idea of using this simple model is that it offers a heuristic setting for our
 178 theoretical barotropic expectations for what may happen in a more complex primitive
 179 equation ocean model with baroclinicity and a shelf (Section 4). Having said this, to

emphasize the relevance to the reader, this section does highlight some of the complex model results from Section 4 as appropriate. Our 2D, non-dimensionalised¹ equations are:

$$fk \times \mathbf{u} = -\nabla p - r\mathbf{u} + \tau_x$$

$$\nabla \cdot \mathbf{u} = 0$$

where f is the Coriolis parameter – negative for the Southern Ocean, \mathbf{u} is a two-dimensional velocity vector, p is pressure, r is a friction coefficient, τ_x a zonal stress and ∇ operates horizontally. A zonal surface stress (Figure 2), inspired by the observed pattern (Figure 1) is used. Hereafter, ‘surface stress’ and ‘wind stress’ will be used interchangeably. Compared to previous Southern Ocean idealised studies (e.g. *Abernathey et al.*, 2011), the wind stress here includes Easterlies and has a non-zero stress in the South where we imagine an ice shelf front. A change in the boundary condition, from a re-entrant east-west channel to

¹ The non-dimensionalised form is obtained by starting with the dimensional, steady, linear and depth-integrated equations: $H(f\mathbf{k} \times \mathbf{u}) = -H\left(\frac{1}{\rho_0}\nabla p\right) - r\mathbf{u} + \frac{\tau_x}{\rho_0}$ and $H(\nabla \cdot \mathbf{u}) = 0$. Variables are defined as in the main text, additionally H is seafloor depth and ρ_0 is a reference density. We define scales for our non-dimensional variables: $\mathbf{x} = (x, y, z) = (L\hat{x}, L\hat{y}, H\hat{z})$, $\mathbf{u} = U\hat{\mathbf{u}}$, $p = P\hat{p}$ and $\tau_x = \tau_0\hat{\tau}_x$. We treat r and f as our problem’s key parameters and so do not nondimensionalize them. Substitution of these definitions leads to $HU(f\mathbf{k} \times \hat{\mathbf{u}}) = -H\left(\frac{1}{\rho_0}P\hat{\nabla}\hat{p}\right) - rU\hat{\mathbf{u}} + \frac{\tau_0}{\rho_0}\hat{\tau}_x$ and $HU(\nabla \cdot \hat{\mathbf{u}}) = 0$. Now, assuming a leading balance between pressure and the wind stress term, as per Veronis (1966), gives $P \sim \tau_0 L/H$. Following *Bryan* (1963), we assume Sverdrup balance will hold over much of the domain and take $U = \frac{\tau_0}{\rho_0 \beta HL}$, where $\beta = \frac{\partial f}{\partial y}$. Substitution of these two relationships into our two latest equations, with some cancellation gives: $\hat{f}\mathbf{k} \times \hat{\mathbf{u}} = -\hat{\nabla}\hat{p} - \hat{r}\hat{\mathbf{u}} + \hat{\tau}_x$ and $\nabla \cdot \hat{\mathbf{u}} = 0$, where $\hat{f} = \frac{f}{\beta L}$ is the nondimensional Coriolis frequency and $\hat{r} = \frac{r}{\beta HL}$ is the nondimensional bottom friction. For convenience we drop the circumflex accent in the main discussion.

a wall, leads to fundamental changes in the circulation (Section 2a). We discuss throughflow and gyre regimes in terms of the pictured layers in Figure 2: top (τ_x/f) and bottom ($-ru/f$) Ekman, and geostrophic ($-\nabla p/f$) transports. The full transport, the sum of the 3 layers, is shown in Figure 3. Note that, here, all 3 layers are really taking place in one slab of fluid and the transports in the pictured layers are diagnostic. Circulation in the top Ekman layer is common to both regimes, but the means by which the lower layers balance the momentum input is different due to the change in boundary condition (Section 2a). Practically, for Figure 2 and 3, variables u , v and p are solved with a finite element method in Mathematica, then the Ekman and geostrophic transports are found diagnostically using the above relations. In Section 2b, we use these equations to study the changes in a throughflow and gyre regime under a constant offset in winds. In Section 4, we will return to these ideas but with a primitive equation ocean model with discrete z^* -levels which solves a depth-dependent momentum equation. The simple approach used here highlights the linear dynamics relevant to our wind shift experiments in Section 4 and shows how a prescribed wind stress sets up the circulation in the lower layers.

a. Commonalities and differences to both throughflow and gyre regimes.

As pictured in Figure 2, in both throughflow and gyre regimes, the top (near surface) Ekman transport is the same. In the Southern hemisphere, the top Ekman transport is directed 90° degrees to the left of the surface stress and surface Ekman suction and pumping arises due to divergences and convergences (respectively) in the near-surface Ekman transport (e.g. Karnauskas 2020). Here, a change from cyclonic to anti-cyclonic wind stress curl leads to a change from upwelling to downwelling regions either side of the maximum westerlies. We thus expect upwelling South of the peak westerlies and downwelling to the North. Approaching the boundaries for the ‘control’ wind stress shown, the curl goes to zero in the South but is non-zero in the North, hence, only the Northern boundary will have curl driven downwelling. We have no normal flow conditions at the Southern and Northern boundaries, so at the Southern wall the non-zero Easterly wind by continuity leads to downwelling. In contrast, the Northern wall goes to zero stress and so the wind *at the boundary* does not drive ‘continuity driven’ downwelling. We will return to these ideas when considering wind shifts.

In a throughflow regime, the top Ekman transport leads to a meridional pressure gradient that drives geostrophic currents that match the wind direction (Figure 2 throughflow,

geostrophic layer), this is enabled by the re-entrant boundary. The bottom Ekman transport then flows to the right of the geostrophic transport returning the flow transported by the top Ekman layer (Figure 2 throughflow, meridional transport panel). Here, a Stommel linear friction is used so the bottom Ekman transport is 90° degrees to the right of the geostrophic transport (rather than 135° for the Ekman solution; *Olbers et al.* 2012). Top and bottom Ekman pumping and suction balance locally so there is no vertical stretching or squeezing of fluid columns and the flows are purely zonal. Thus, in a zonally averaged throughflow regime, we have clockwise and anti-clockwise overturning cells where the latitude of zero wind stress, delineates the boundary between the two cells that are driven by the Westerly and Easterly winds, respectively.

In a gyre regime, the no normal flow condition of the eastern and western boundaries results in dramatic changes. In the geostrophic layer, the depth-integrated circulation consists of a balance between the meridional advection of planetary vorticity and the wind stress curl (i.e. Sverdrup balance); in the return flow boundary layer, the advection of planetary vorticity is balanced by the curl of bottom friction (e.g. Waldman & Giordani 2023). As in the throughflow case, the top Ekman transport is prescribed, this sets off an identical top Ekman pumping and suction pattern where the resulting circulation is now constrained by walls on all sides. Since the geostrophic flow is largely horizontally non-divergent, Ekman pumping/suction through the top and bottom Ekman layers results in stretching and squeezing of fluid columns in the geostrophic layer (McWilliams, 2011; Pedlosky, 1996). The sum of the Ekman and geostrophic components gives the depth-integrated transport. Unlike in a throughflow regime, a gyre regime has geostrophic zonal and meridional flows that are non-uniform in x . Also unlike in a throughflow regime, the meridional return transport is no longer confined to the bottom Ekman layer but also to the geostrophic return flow (Figure 2 gyre, meridional transport panel). This is because in a throughflow regime, there is no western wall to support a pressure gradient and so there can be no geostrophic meridional transport.

b. *Linear responses of both systems to wind shifts.*

In this section, we apply a constant positive, zonally uniform change in wind stress of 0.8 to the system considered in Section 2a (Figure 2); *CTRL* and *CTRL* + 0.8 are shown in Figure 3. As the perturbation is a constant offset of the wind profile (top row overlay Figure 3), the wind stress curl does not change. In an idealised sense, this is similar to what we expect with climate change; an increase in the strength of the westerly winds, a weakening of the easterlies and a shift of the easterly-westerly transition zone south. Changes in the top Ekman layer are common to both regimes (Figure 3e-h), but the means in which the lower layers balance the momentum input is different due to the different boundary condition. In a throughflow regime, as 0.8 is added to the wind stress (column 2 Figure 3), the north-south sea surface height gradient associated with the zonal geostrophic flow gets stronger and so it directly modifies the strength of the zonal geostrophic currents (see also Section 4c and Figure 10). In a gyre regime however, the *zonal* Sverdrup transport is related to *the gradient* in the wind stress curl, and thus the zonal transport is locked. In both regimes, the curl is not changing so neither can the region or magnitude of upwelling and downwelling. The magnitude of Ekman transport does change, so by continuity, the downwelling transport at the northern and southern boundaries has to change, and in this instance an increase in one leads to a compensating decrease in the other.

In a throughflow regime, the eastward and westward jets associated with the eastward and westward stresses increase and decrease in strength (respectively). When 0.8 is added to the wind stress, the geostrophic eastward jet accelerates leading to the bottom Ekman transport commensurately increasing (Figure 3r). Most importantly, the two Ekman overturning cells described earlier in this Section shift south (Figure 3e-f, m-n, q-r). Since the latitude of the easterly-westerly transition zone has shifted south, the upwelling of the northern cell has also shifted south; this change will be a crucial feature in our numerical experiments in Section 4. So how is it that a change in surface stress can have such a dramatic effect in a throughflow regime as compared to a gyre?

Veronis (1996) and *Vallis* (2017) provide some clues for how we can understand the gyre regime response. Consider the case of a uniform, zonal, eastward wind applied to the gyre case. That would set up a northward Ekman transport which would drive an eastward

geostrophic current. The eastward geostrophic current would create a raised sea surface height in the east, driving a geostrophic current southward². Bottom Ekman transport aside, this geostrophic current would return the volume displaced by the original northward Ekman transport. At equilibrium, there would be no zonal flow, and hence no meridional bottom Ekman transport, but there would be a closed meridional overturning circulation with northward transport in the surface Ekman layer balanced by a southward geostrophic flow set up by the west-east gradient in sea surface height. Moreover, if we were to uniformly increase the strength of the wind, at equilibrium, we would only expect an increase in the west-east gradient of sea surface height (21.7.6 in *Vallis* (2017)) and an associated increase in the meridional overturning. Returning to the wind stress in Figure 3, since the total circulation streamfunction is determined by the curl of the stress and our constant offset (0.8) has no curl, it does not change the total streamfunction (Figure 3c-d). Exploiting our simple previous example, the sea surface height gradient *change* only depends on the sign of offset, not on the direction of the winds. Moreover, for the total streamfunction to not change (Figure 3c-d and Figure 11 bottom row), the vertical structure of the flow has to compensate via a change in upwelling or downwelling at the northern and southern walls (see also Figure 10 bottom row).

Veronis (1996) shows that a constant offset of the stress effects both the Ekman and geostrophic transports in a compensating manner (Figure 3s-t), whilst very large offsets are explored we will consider smaller changes in this study. *Veronis* (1996) suggests that the compensation occurs equally between geostrophic and a top Ekman component, bottom Ekman is not considered. Since the zonal Sverdrup transport is related to the gradient in the wind stress curl and here, we only have zonal winds, the geostrophic compensation will occur in the meridional transport. In Figure 3, two right columns, as we add 0.8 to the forcing: the

² In contrast, in the throughflow case, the increased zonal momentum input is balanced by stronger bottom friction.

top Ekman transport moves uniformly up as the geostrophic transport uniformly shifts down to compensate (Stommel, 1957, and Figure 3s-t). Spatially, we see that the geostrophic transport entirely compensating for changes in the top Ekman transport is accomplished by a re-arrangement of the northern gyre (Figure 3k-l). With this kind of forcing change and model formulation, there is no change of the bottom Ekman because there is no change in curl and the bottom Ekman transport depends on $-ru/f$.

The consequences of this simple barotropic linear theory will now be explored in a primitive equation ocean model (e.g. Figure 6), of key interest is how a more sophisticated numerical model (e.g. baroclinicity, non-linear momentum, shelf break and deep ocean ridge, combination of flow regimes etc) will add complexity to the response.

3 Model and experimental design

a NEMO model configuration

The ocean general circulation model used in this study is version 4.0.4 of the Nucleus for European Modelling of Ocean model (NEMO; *Gurvan et al. (2017)*). NEMO solves the incompressible, Boussinesq, hydrostatic primitive equations with a split-explicit free-surface formulation. NEMO here uses a z^* -coordinate (varying cell thickness) C-grid with partial cells at the bottom-most and top-most ocean layers in order to provide more realistic representation of bathymetry (Bernard et al., 2006). Our model settings include: a 55-term polynomial approximation of the reference Thermodynamic Equation of Seawater (TEOS-10; IOC and IAPSO (2010)), nonlinear bottom friction, a free-slip condition at the lateral boundaries, energy- and enstrophy-conserving momentum advection scheme and a prognostic turbulent kinetic energy scheme for vertical mixing. Laterally, we have spatially varying eddy coefficients with a Laplacian operator for iso-neutral diffusion of tracers and a biharmonic operator for lateral diffusion of momentum.

Symbol	Value	Description
L_x, L_y	2003.7, 3025 km	Domain size
H	3047 m	Depth of domain

Δ_x, Δ_y	7.9 km	Horizontal resolution
Δ_z	1 m surface – 135 m depth	Vertical resolution
f_0	$-1.46 * 10^{-4} s^{-1}$	Southern boundary Coriolis
f_y	$-1.28 * 10^{-4} s^{-1}$	Northern boundary Coriolis
L_{EW}	770 km	Value of y where winds transition from easterly to westerly
$L_{easterlies}, L_{westerlies}$	385, 2239 km	Distance over which the easterly and westerly winds blow
τ_E, τ_W	-0.05, 0.2 N m ⁻²	Peak easterly and westerly wind stress
eiv	2000 m ² /s	GM constant Eddy Induced Velocity (eiv) parameterisation

Table 1. Key parameters used in the configuration with model reference winds (τ_0).

The modelling setup is pictured in Figure 4 with key parameters in Table 1. The modelling domain is on a β -plane with 257 x 385 regularly spaced points in x and y, respectively. The relatively coarse resolution of the model (7.9 km) was necessary here due to the high number of simulations (next sub-section). *Stewart and Thompson (2015)* found that 1km or finer is required to resolve the eddies for cross-shelf heat transport. However, on the larger scale, *Stewart and Thompson (2012)* found that 5 km was sufficient to resolve the Easterly eddy overturning on the shelf. Here, to mitigate our lower resolution, we use the Gent-McWilliams Eddy Parameterization (GM; *Gent et al., 1995; Gent & McWilliams, 1990*) to represent the effects of unresolved mesoscale eddies on tracer distribution, i.e., temperature, salinity and other tracers. We choose $eiv = 2000 m^2/s$ based on *Allison et al. (2011)* and *Visbeck et al. (1997)*. The ocean floor is limited to 3023 m and is represented by 61 vertical levels, where the vertical grid is $\sim 1m$ at the surface and 135m at the lowest level with initial thicknesses taken from the 75-level DRAKKAR formulation used in realistic configurations (e.g. ORCA025). Walls exist on the northern and southern boundaries in all experiments. The western-eastern boundary is fully re-entrant but in some cases is effectively

blocked, Figure 4 for example is effectively in a gyre regime due to a wall at 405 km. The external forcing is a restoring condition (towards the initial state) at both the northern boundary and near surface, additionally, there is a surface wind stress (Figure 4). The simulations are initialised from rest with initial conditions derived from World Ocean Atlas 2018 (WOA; Boyer, Tim P. et al., 2018), these fields are then set as the surface restoring condition as the simulation evolves. The northern restoring condition is shown in the Figure 1 insets (7 day restoring timescale), it is found by taking the WOA zonal average of profiles along the Subantarctic Front from *Park et al.* (2019), pictured in green in Figure 1a. The near-surface restoring is then found by taking the surface WOA zonal average of temperature/salinity in-between the Antarctic coast and the Subantarctic Front, normalising for NEMO's grid points. Similar to other studies in the literature (Wilson et al., 2022; Zhai & Munday, 2014), here, we use a 10m restoring thickness and 10 day restoring timescale. The configuration has no: ice-shelf, sea ice and tides, but is inspired by previous southern ocean idealised channel modelling (e.g. Abernathey et al., 2011; Morrison et al., 2011), where the interest here was to have a simple system in which to understand the momentum balance's role in setting shelf properties from wind stress forcing alone. All simulations in this paper have a spin-up of 90 years where the time-mean values of a further 10 years are used for all analysis. Spin-up metrics including domain averaged SSH and domain integrated salinity, temperature and kinetic energy, combined with test simulations of 370 years, suggest that the 90 year spin-up is sufficient to capture the equilibrated response of the ocean circulation to the forcing.

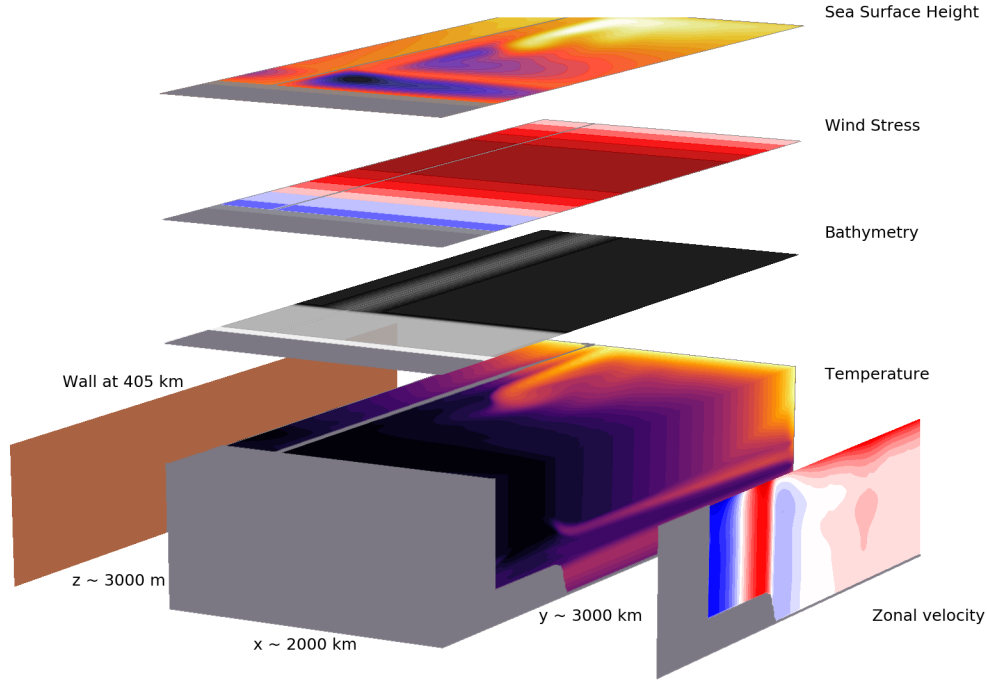


Figure 4. A 3D snapshot of the model's temperature field from a gyre experiment. The temperatures range from -1.9 to 1.5 °C. Overlaid, above: sea surface height (-5 to 20 cm), control wind stress (τ_0 ; -0.05 to 0.2) and bathymetry; right: zonal mean zonal velocity (-20 to 20 cm/s); left: most experiments have some kind of wall at 405 km rising from either the shelf or deep ocean ridge, here, there is a wall the full length of the domain. Note the vertical scale is stretched.

b Experiment design

1) SURFACE FORCING AND BATHYMETRY

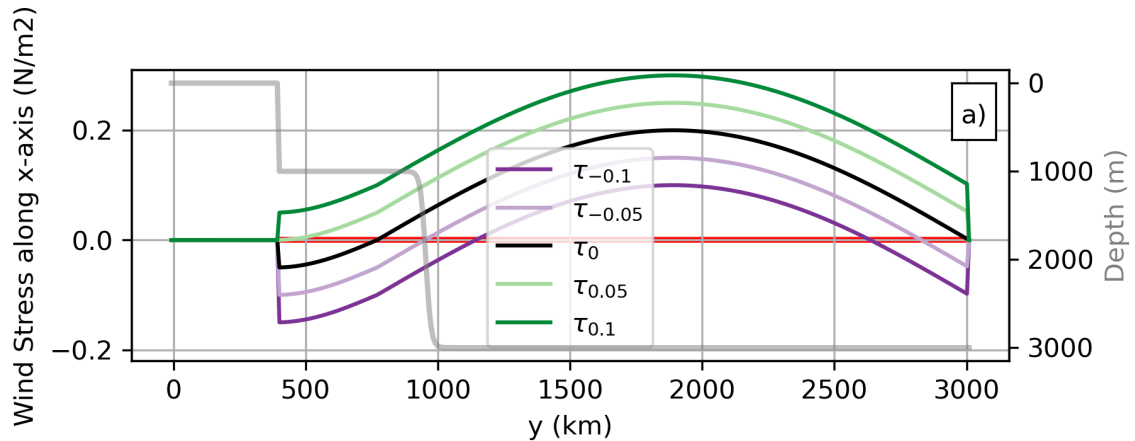
Given the idealized nature of this study, we choose an idealized surface forcing and boundary conditions. The wind stress forcing is the same zonally throughout the domain (meridional wind stress is zero) and is intended to represent a zonal average of the Southern Ocean's easterlies and westerlies (Figure 1b; JRA55-do (Tsujino et al., 2018)):

$$\tau_c(y) = \begin{cases} 0, & 0 < y < 393 \text{ km} \\ \tau_E * \sin\left(-0.5 \pi y / L_{\text{easterlies}}\right) + c, & 393 \leq y \leq 770 \text{ km} \\ \tau_W * \sin\left(\pi y / L_{\text{westerlies}} - L_{EW} \pi / L_{\text{westerlies}}\right) + c, & 770 \leq y \leq 3025 \text{ km} \end{cases}$$

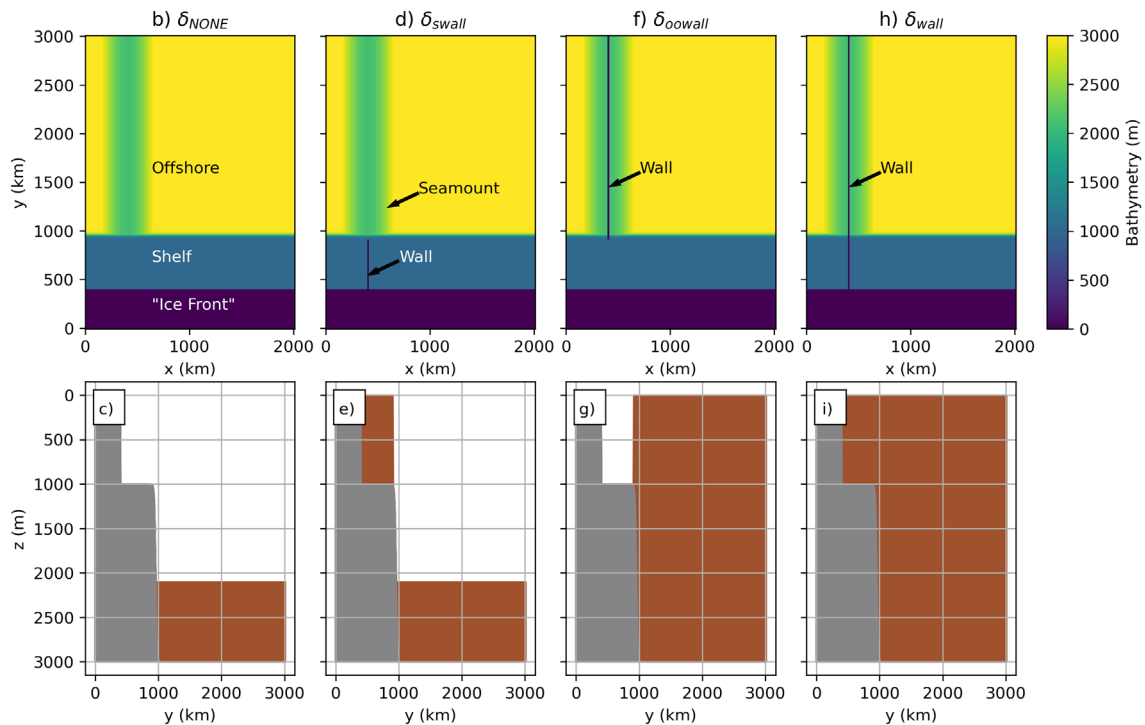
$c = 0$ is the control simulation (τ_0). Four additional values of c give the four perturbation forcings: $\tau_{-0.1}$, $\tau_{-0.05}$, $\tau_{0.05}$, $\tau_{0.1}$. The wind stress fields used are shown graphically in Figure 5a. To emulate the geometry of the Southern Ocean (see Figure 1a and Section 1 discussion), we then have four different bathymetries (Figure 5 middle and bottom row). All bathymetries

have the same deep ocean 900m high meridional ridge (Figure 5b,d,f,h), sea floor and zonally uniform shelf (gray line Figure 5a). The first case (δ_{NONE}) only consists of the ridge and shelf, whereas cases 2-4 (δ_{swall} , δ_{oowall} , δ_{wall}) have a wall at 405 km that is two grid cells wide and rises out of the top of the deep ocean ridge. Since the western-eastern boundary is re-entrant, the construction of a wall is effectively changing the boundary condition. Thus, in the case of δ_{NONE} we are in a throughflow regime and in δ_{wall} gyre regime. The remaining other two cases will lead to combinations of regimes, namely, δ_{swall} will have a gyre on the shelf/throughflow offshore whereas δ_{oowall} will have a gyre offshore/throughflow on the shelf, respectively.

407



408



409

Figure 5. a) Five zonally uniform wind stress forcings applied to each of the 4 bathymetries (lower panels); black (τ_0) is the control simulation and perturbation experiments are created by adding ($\tau_{0.05}$, $\tau_{0.1}$) or removing ($\tau_{-0.05}$, $\tau_{-0.1}$) a constant. Red horizontal line at zero highlights transition from easterlies to westerlies, where applicable. Gray line (twin axis, scale on right) shows the shelf, common to all experiments (i.e. δ_{NONE}). Middle and bottom rows show the 4 different bathymetries (δ_{NONE} , δ_{swall} , δ_{oowall} , δ_{wall}) used to create different “boundary conditions”. b-i) Prescribed bathymetry used for experiments 1-20 experiments (surface forcing shown in Figure 1), each column is a new bathymetry. Middle row: plan view. Bottom row: meridional slice where gray shows the bathymetry (unchanged across all bathymetries) and brown shading (b-d) shows the wall at $x = 405$ km (approx). All experiments are listed in Table 2.

420

421

2) EXPERIMENTS

From Figure 5, we have five different surface forcings (Figure 5a; $\tau_{-0.1}$, $\tau_{-0.05}$, τ_0 , $\tau_{0.05}$, $\tau_{0.1}$) and four different bathymetries (Figure 5 middle and bottom row; δ_{NONE} , δ_{swall} , δ_{oowall} , δ_{wall}), taking the combinations leads to 20 experiments (Table 1). The simulations are designed to highlight the dependence of the strength and location of the ASF to changes in boundary condition and changes in surface forcing.

Number	Name	Boundary condition is				Surface Forcing (c)
		Fully Open	Shelf Block	Deep Ocean Block	Fully Closed	
1	$\delta_{NONE}\tau_{-0.1}$	✓				-.01
2	$\delta_{NONE}\tau_{-0.05}$	✓				-0.05
3	$\delta_{NONE}\tau_0$	✓				0
4	$\delta_{NONE}\tau_{0.05}$	✓				.05
5	$\delta_{NONE}\tau_{0.1}$	✓				.1
6	$\delta_{swall}\tau_{-0.1}$		✓			-.01
7	$\delta_{swall}\tau_{-0.05}$		✓			-0.05
8	$\delta_{swall}\tau_0$		✓			0
9	$\delta_{swall}\tau_{0.05}$		✓			.05
10	$\delta_{swall}\tau_{0.1}$		✓			.1
11	$\delta_{oowall}\tau_{-0.1}$			✓		-.01
12	$\delta_{oowall}\tau_{-0.05}$			✓		-0.05
13	$\delta_{oowall}\tau_0$			✓		0
14	$\delta_{oowall}\tau_{0.05}$			✓		.05
15	$\delta_{oowall}\tau_{0.1}$			✓		.1
16	$\delta_{wall}\tau_{-0.1}$				✓	-.01
17	$\delta_{wall}\tau_{-0.05}$				✓	-0.05
18	$\delta_{wall}\tau_0$				✓	0
19	$\delta_{wall}\tau_{0.05}$				✓	.05
20	$\delta_{wall}\tau_{0.1}$				✓	.1

Table 2. List of Experiments. Name indicates the bathymetry (δ) and surface forcing (τ_c) used where $c = 0$ is the control surface forcing. See Figure 5 for details.

4 Numerical Results

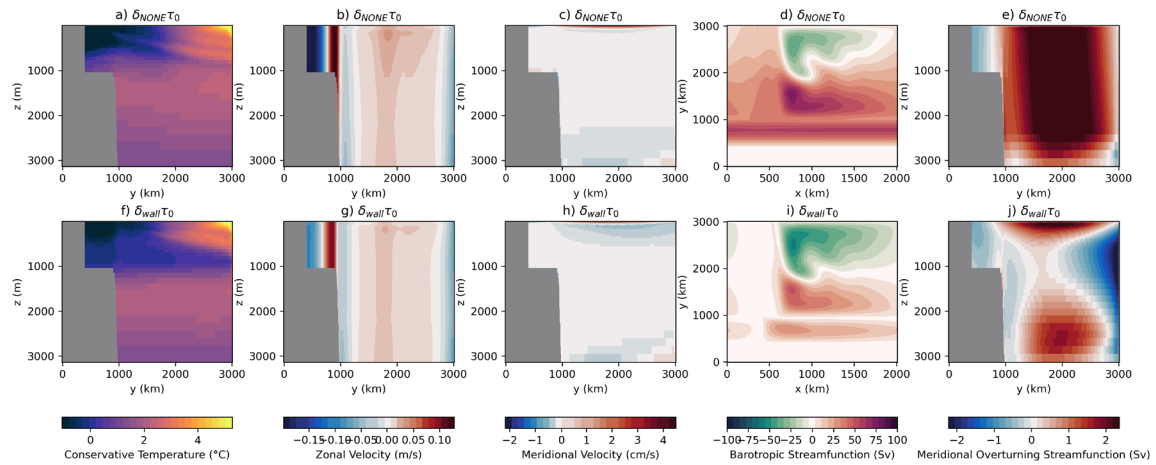


Figure 6. Overview of the mean state of the open (first row; δ_{NONE}) and closed channel (second row; δ_{wall}) with control wind stress (τ_0). Along the columns: Conservative Temperature ($^{\circ}\text{C}$), Zonal Velocity (m/s), Meridional Velocity (cm/s), Barotropic Streamfunction (Sv) and Meridional Overturning Streamfunction (Sv) where the first 3 are the zonal average.

a Summary of NEMO's mean state circulation for throughflow and gyre regimes.

Figure 6 shows mean circulation metrics of the two “bookend” cases with a control surface stress, namely, $\delta_{NONE}\tau_0$ which is in a throughflow regime and $\delta_{wall}\tau_0$ which is in a gyre regime. Comparing Figure 6a,f the throughflow case has relatively warm waters on the shelf compared to the gyre regime case. The circulation metrics in the subsequent columns are broadly consistent with the linear circulation discussed in Section 2 (Figure 2), although the addition of more complex physics and geometry does lead to some new features. Having added a ridge in the deep ocean, the barotropic streamfunction in the open channel (Figure 6d) has partially blocked flow over the ridge and unblocked throughflow on the shelf. In contrast the closed channel (Figure 6i), has gyres both on the shelf and in the deep ocean. In Figure 6i, compared to Section 2a, the addition of a shelf introduces steep f/h gradients, leading to an additional gyre in the south (same direction as the curl is unchanged over that region). Figure 6d,i also have non-linear, eddy features (standing eddies, meanders and eddy-recirculation) in-between the gyres due to vorticity transport (Stewart et al., 2021). Comparing Figure 6b,g, the zonal flows in Figure 6g are consistent with the three gyres observed in Figure 6i, or like Figure 2 but with the additional gyre on the shelf. Relatedly, Figure 6b,d, is not like Figure 2 as a throughflow, because the zonal flows are dominated by

the gyres created through the deep ocean ridge. Sensitivity tests highlight that the zonal flow (Figure 6b) does look like Figure 2 (left) in the absence of the ridge (not shown).

Looking at the meridional velocities in Figure 6c,h, transport in the top and bottom Ekman layers is also consistent with Section 2a. In particular, the latitude in which the transport changes direction in the top and bottom layers in a throughflow regime coincides with the change in the wind direction. As expected, in a throughflow regime, the return flow is confined to a bottom Ekman layer on the shelf, and distributed over the height of the seamount (900 m) in the deep ocean, whereas in a gyre regime the geostrophic return flow is higher in the water column. Considering the Eulerian overturning streamfunction, for a throughflow regime (Figure 6e), we have clockwise and anti-clockwise overturning cells that are separated by the change in wind direction. For a gyre regime (Figure 6j), two similar cells are much closer to the surface and we have an additional 3 sub-surface cells that arise from the change in zonal currents (Figure 6g).

b Shelf temperatures are modulated by winds and circulation regime

Understanding how temperature on the shelf changes (Figure 7-8) as the ocean circulation changes across all the experiments in Table 2 (Figure 9-14), is a key objective of this study. Figure 7 shows the shelf response in terms of zonally averaged temperature and Figure 8 highlights the heat that is available on the southern boundary to be transported beneath an imagined ice shelf (not represented here but planned as future work). Figure 7 shows that there are two mechanisms by which the strength and structure of the warm water inflows on the shelf can be altered, by shifting the winds (Figure 7 columns) or by creating a gyre via a change in the boundary constraint (Figure 7 rows). Looking down any Figure 7 column where the coastal downwelling is fixed, we note that the boundary constraint is a key factor in determining the intensity and location of the ASF. For example, focusing on the central column (control wind stress; τ_0), the warmest waters reach the southern boundary when the shelf has a wall (Figure 7h) whereas the presence of a deep ocean gyre (fully blocked offshore), reduces the temperature of warm waters on the shelf (Figure 7c,m). The blocked shelf cases (Figure 7 second row; δ_{swall}) are warmer than the re-entrant cases (Figure 7 first row; δ_{NONE}) since the gyre on the shelf creates a return flow that is driven by the zonal geostrophic currents (Figure S2), in particular, the eastward current near the shelf edge drives a southward geostrophic current which enables warm water inflows. Additionally, the winds are another key constraint, looking left to right *across the rows*, a southward shift in the

transition zone from westerlies to easterlies increases the intensity of warm waters on the shelf (see also Figure S1). This shift is most effective, however, when the winds are shifted over an open channel region (Figure 7 rows 1-3) where the northern Ekman overturning cell's upwelling region is shifted south of the shelf break. This process was outlined with linear theory in Section 2b (Figure 3), namely, in a throughflow regime, as a positive offset is added, the upwelling associated with the northern Ekman overturning cell shifts south. In short, the presence of a wall increasingly hinders the capacity of the winds to drive warmer waters across the shelf and so the winds are maximally effective in a fully throughflow regime (Figure 7a-e; δ_{NONE}). The other extreme then, is the introduction of a full north-south wall (Figure 7 row 4; δ_{wall}) where changes in the winds are no longer able to (dramatically) change the location of the ASF. This is due to there being no change in the (total) horizontal circulation in the presence of a wall because, by design, changes in τ_c do not change the wind stress curl, how this is achieved baroclinically is discussed in Section 4d. Finally, a wall in the deep ocean (Figure 7 row 3; δ_{oowall}) flattens isotherms in the deep ocean thus reducing the amount of available heat close to the shelf break to be brought up onto the shelf when the winds are shifted.

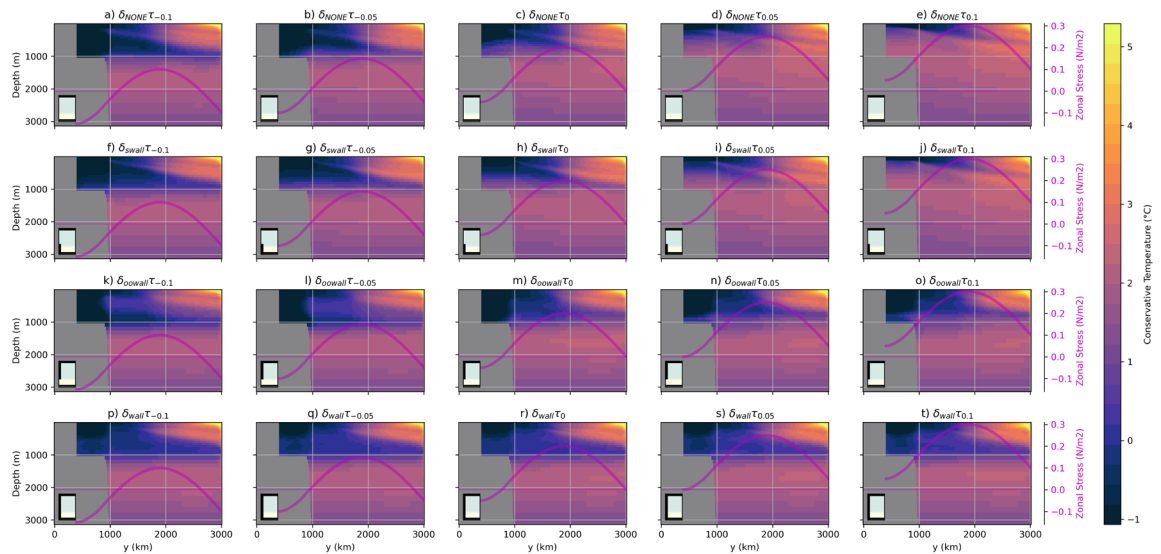


Figure 7. Zonal mean temperature for all experiments (Table 2). Each column has a new wind stress forcing (Figure 5a) where the middle column is the control wind stress. The magenta line highlights the zonally averaged wind stress. Each row has a different boundary condition, in order: i) fully re-entrant, ii) blocked shelf, iii) blocked deep ocean and iv) fully blocked shelf and deep ocean, respectively. The small glyphs (bottom-left) schematically indicate the geometry under consideration in each panel. This panel-experiment layout applies to Figures 7-12 and S1-S4.

Sub-surface temperature changes at our imagined ice front are particularly relevant to ice shelves, so Figure 8, refines our focus towards the zonal temperature changes at the southern boundary. Due to the presence of a wall and changes in top-layer Ekman transport, we do expect and observe differences in downwelling at the southern boundary (e.g. Figure 8f-h). Comparing rows, the shelf gyre is important by the warmer ice front temperatures in Figure 8f,g,h as compared to the runs without a wall on the shelf (Figure 8a,b,c,k,l,m). In these instances, the wall on the shelf provides the most effective transport of shelf edge temperatures to the ice front by enhancing the cross-shelf transport of waters, only in the presence of a wall is there any meridional geostrophic flow. When the shelf is open (row 1 Figure 8), waters cannot cross the shelf edge so effectively, so even when the winds push warm waters onto the outer shelf, they do not get to the ice front. The deep ocean gyre's importance is readily seen by comparing the δ_{wall} simulations (Figure 8 row 4) with the other boundary conditions (Figure 8 rows 1-3), the δ_{wall} simulations have a zonal structure and temperature variability with depth. The caveat is that the deep ocean gyre is only important when both the shelf *and* deep ocean is blocked (comparing Figure 8 rows 1,3 and rows 2-4), it is evidently non-linear. As compared to Figure 7, Figure 8 shows nuanced changes with the δ_{wall} simulations in terms of the zonal temperature structure (Figure 8 row 4). Figure 7 row 4 suggests that δ_{wall} removes almost any sensitivity to changes in wind stress (Figure S1 shows a weak sensitivity). Figure 8 however shows zonal changes with a small increase in temperature at the eastern boundary and along the shelf sea floor as a constant offset to the winds is added (Figure 8 bottom row). This is likely driven by the increase in coastal downwelling and the change in southward meridional geostrophic transport highlighted in Section 2b, the underlying dynamics will be re-visited with new circulation metrics in Section 4c and 4e (Figure S5).

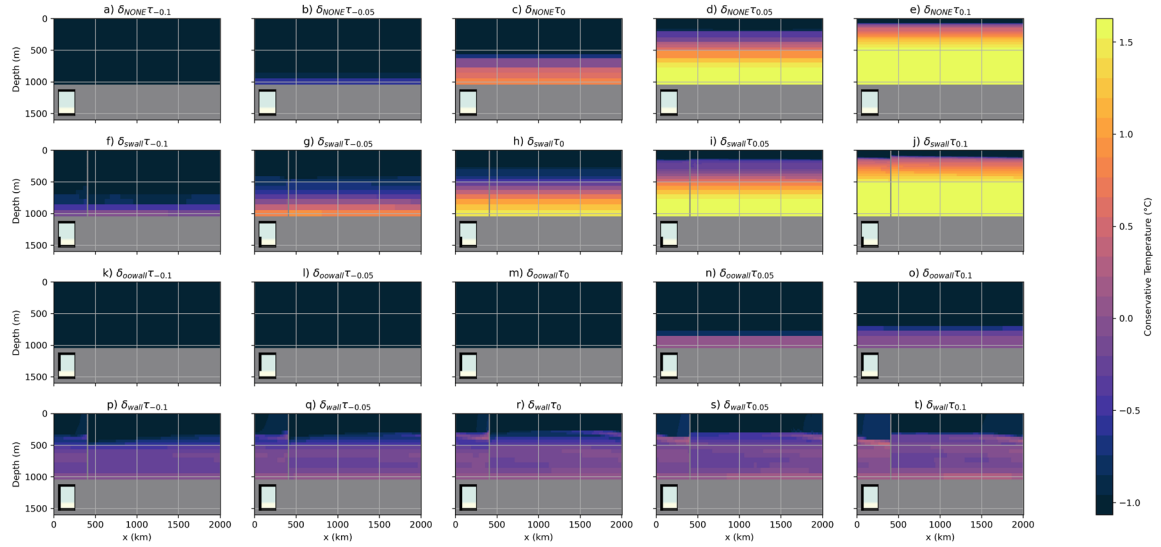


Figure 8. Same panel-experiment layout as Figure 7 but for southern boundary ("Ice Front" indicated Figure 5b) mean temperature.

c Understanding horizontal circulation changes due to winds and circulation regime

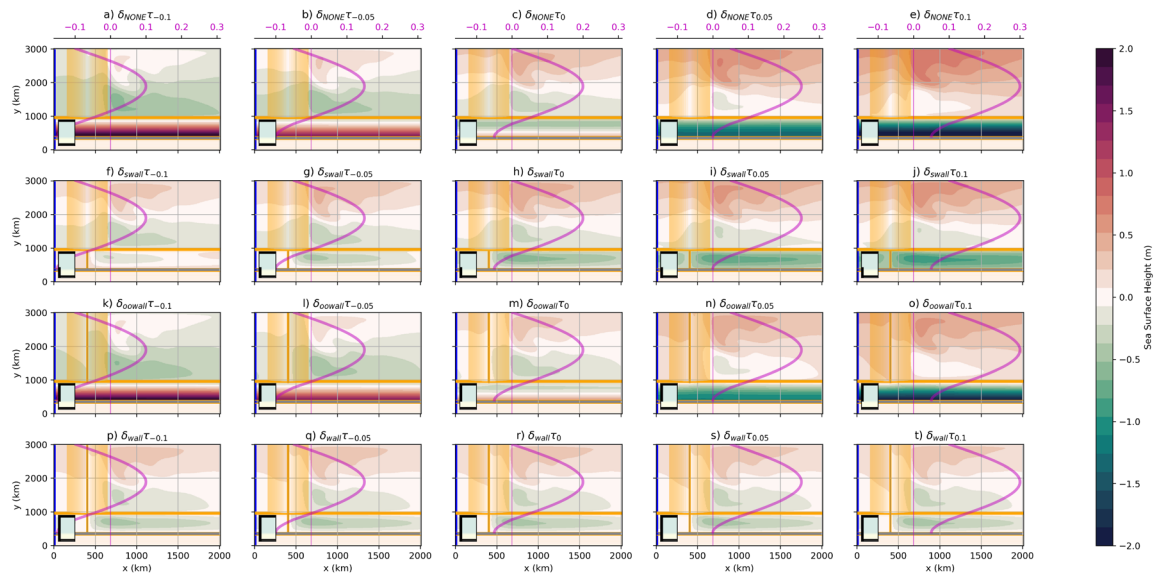


Figure 9. Same panel-experiment layout as Figure 7 but for sea surface height for all experiments. Thin yellow lines are isobaths.

This section characterizes the horizontal circulation (SSH in Figures 9-10 and barotropic streamfunction in Figure 11) changes that lead to the described differences in shelf temperatures (Section 4b). Similarities and differences to the linear response (Section 2) are also highlighted when relevant.

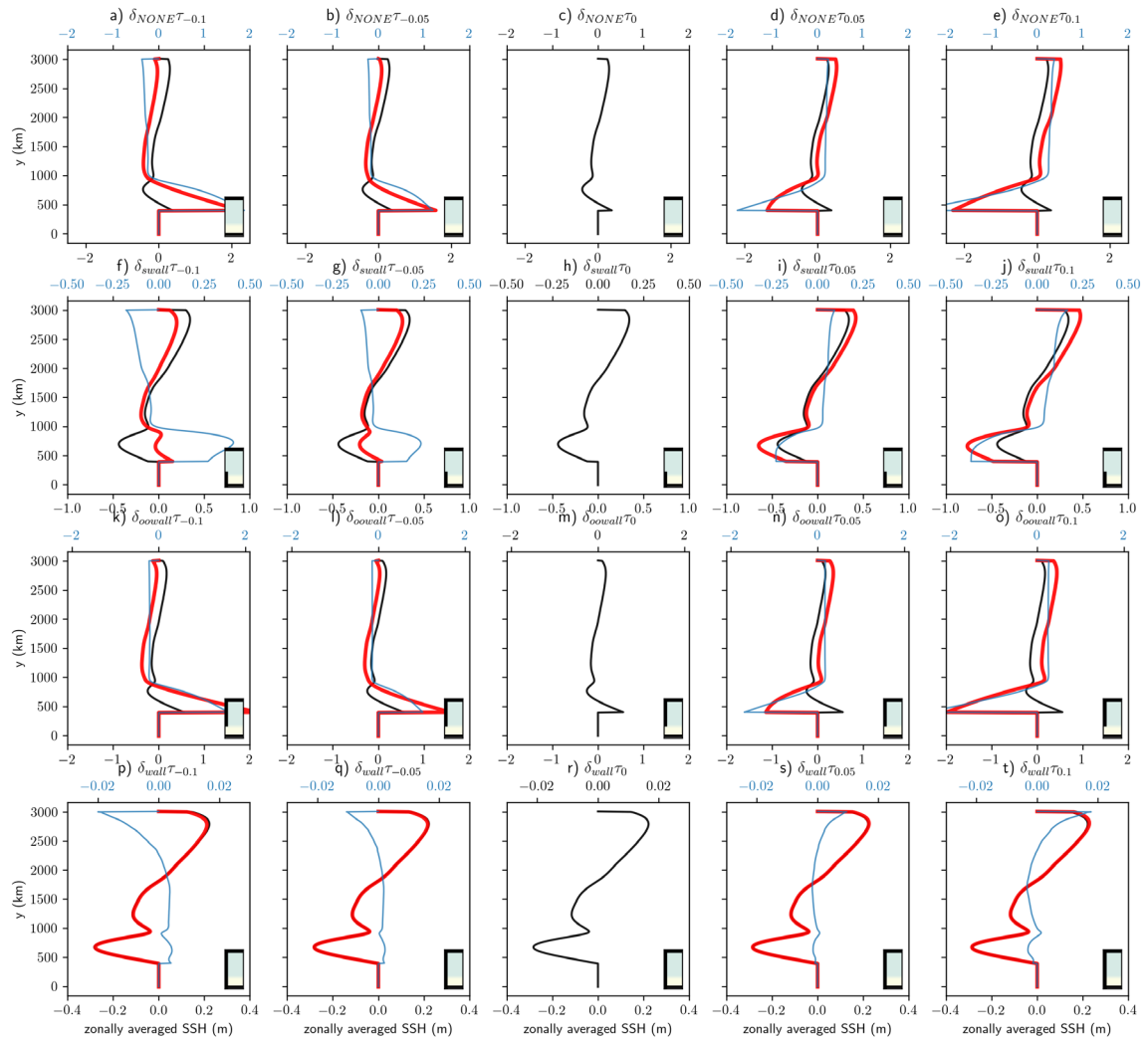


Figure 10. Zonal mean sea surface height for all experiments with same panel-experiment layout as Figure 7. In all panels, black is the control simulation (wind stress offset $c=0$) where the control experiment changes on each row. The red line is the perturbed stress experiment and the blue is the difference between the two (top; alternative x-axis with blue scale). If comparing between rows, one should focus on the red lines in the perturbed experiments and the black line for the central column, also note the differing scales on domain axis.

Figures 9-10, like Figure 3i-l, highlight how the near-surface geostrophic transport responds to changes in boundary conditions under the same top Ekman transport. Like in Section 4a, we start with the two “bookend” cases ($\delta_{NONE}\tau_0$ and $\delta_{wall}\tau_0$). Comparing Figure 9c,r, due to the deep ocean ridge blocking the barotropic flow, the throughflow case is dominated by the influence of the gyre regime (the shelf region is the exception). In the control throughflow and gyre cases, the north-south SSH gradient (Figure 10c,r) is non-linear as the stress has curvature and f is varying. We now briefly consider the ‘full’ throughflow (δ_{NONE}) and gyre geometries (δ_{wall}) response to a change in surface forcing. A throughflow regime’s response (top row Figure 9) is readily understood by considering the simpler case of when the stress is only eastward ($\delta_{NONE}\tau_{0.05}$ and $\delta_{NONE}\tau_{0.1}$ in Figure 9d-e), or mostly

eastward in the barotropic model (columns 1-2 in Figure 3). In these cases, driven by northward Ekman transport (Figure 3e-f), we have a positive SSH offset in the deep ocean (Figure 10d-e). Also note in Figure 10d-e, as compared to the control case, the largest SSH change occurs over the shelf due to the change from easterlies to westerlies over the shelf, this change is relatively large due to the shelf having a flat-bottom. Looking across the whole top row of Figure 9, the strength and positions of the westward and eastward currents on the shelf are modulated by the strength of the wind and the shift in location for the sign change in the winds (see also Section 2b). Moving now to the δ_{wall} geometry's response to a change in surface forcing, since the wind stress curl is unchanged, the barotropic streamfunction is unchanged in the full gyre regime experiments (row 4 in Figure 11 and Figure 3c-d). Further, as expected from Section 2b, the zonal mean SSH at the northern boundary does raise and lower (upwelling/downwelling) as the strength of the offset is increased and decreased (Figure 10 bottom row).

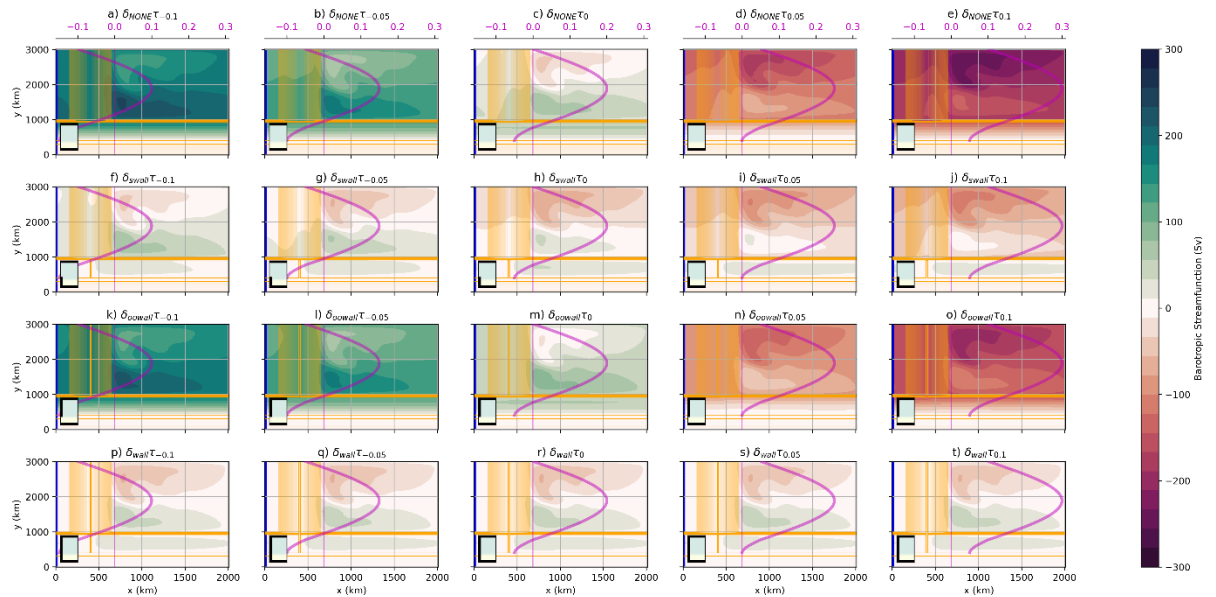


Figure 11. Same panel-experiment layout as Figure 7 but now the Barotropic Streamfunction for all experiments. Thin orange lines are isobaths. The barotropic streamfunction is defined here with $u_{BS} = -\frac{\partial \psi}{\partial y}$ and $v_{BS} = \frac{\partial \psi}{\partial x}$, where they are found from the vertically integrated model transport. In panel r, for example, the streamfunction shows an anti-cyclonic (counterclockwise) gyre in the north and two cyclonic (clockwise) gyres in the south.

We now consider the horizontal circulation changes across all experiments. In all panels in Figures 9-11, a key observation is that the presence of a ridge puts the deep ocean region into a gyre regime. In the absence of a ridge (i.e. a flat bottomed ocean), the deep ocean looks like a throughflow regime from Section 2. Moreover, the ideas from Section 2b (Figure 3) still apply here, it is just that the signal is convoluted by the deep ocean gyres. As an

example, as we add a constant offset to the wind, the eastward flow is accelerated where the contours relating to the gyres are unchanged (e.g. top row in Figure 9,11). With this in mind, note that, both SSH and the barotropic streamfunction (Figure 9 and 11) have the following features: i) rows 1 and 3 are very similar, and ii) row 2 shows modest changes. We consider these two features:

- i) Rows 1 and 3 (throughflow and blocked deep ocean, respectively) in Figure 9 and 11 are similar because the deep ocean ridge blocks the barotropic flow and so creating a wall on top of the ridge only has a limited impact on the large-scale circulation. Namely: deflection/throughflow over the ridge on 1st row as compared to interior return flow in the 3rd row. Additionally, the geostrophic transport on the shelf matches the wind direction (Figure 9) and consistent with Section 2b, the zonally averaged SSH changes commensurately with changes in Ekman transport (Figure 10).
- ii) Due to the shelf being blocked, the barotropic streamfunction (Figure 11) on the shelf for row 2 (blocked shelf) is largely unchanged. However, similar to row 1, the streamfunction shows an eastward acceleration of the deep ocean jet, which is of similar magnitude to row 1 (the streamfunction integrates through a gyre which has both westward/eastward components, reducing the overall transport, see Figure S2). Taking the difference between the streamfunction and SSH (Figure 9), we see that the gyre on the shelf has the same spatial pattern, it is just enhanced by the change in Ekman transport. A positive wind offset has more northward Ekman transport (Figure 10i,j), whereas a negative offset has more southward Ekman transport leading to a weaker dome (Figure 10f,g)

d Understanding overturning circulation changes due to winds and circulation regime

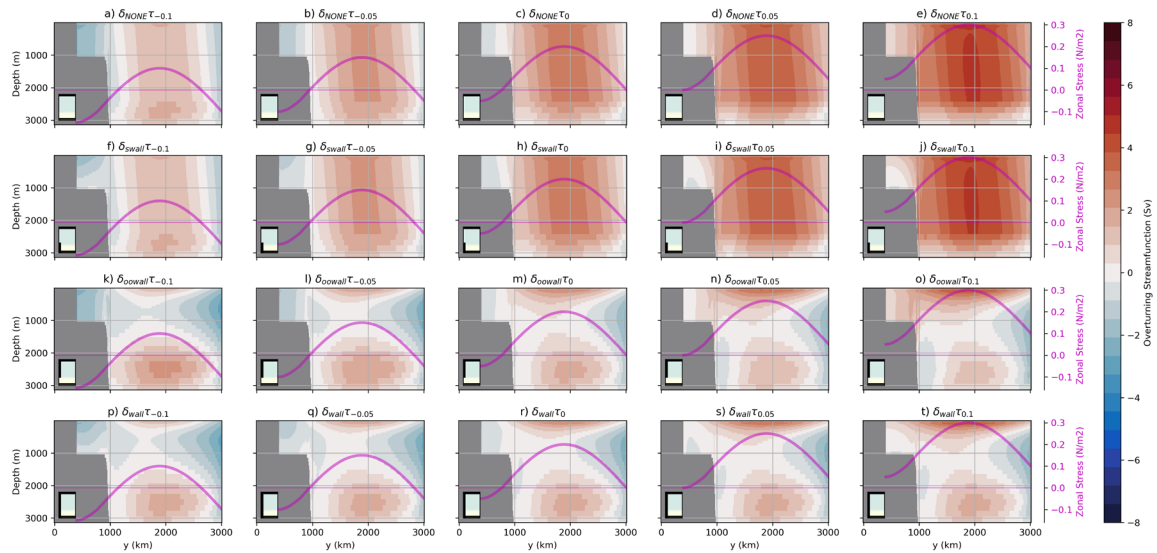


Figure 12. Same panel-experiment layout as Figure 7 but now the Meridional Overturning Streamfunction for all experiments.

The Eulerian meridional overturning streamfunctions shown in Figure 12 highlights how each boundary condition alters the means by which the vertical structure compensates for the changes in top Ekman transport as the stress changes. At the large scale, the overturning is throughflow dominant with boundary condition δ_{NONE} , δ_{swail} (rows 1-2 Figure 12), and gyre dominant for δ_{owall} and δ_{wail} (rows 3-4 Figure 12). Across all regimes, the change in the direction of the top Ekman transport coincides with the latitude at which the winds change direction (e.g. Figure 12c,h,m,r). In a fully throughflow regime (top row Figure 12), the clockwise northern overturning cell (Figure 12a-e) has its geostrophic return flow confined to the height of the ridge. Both the northern and southern (Figure 12a-c) overturning cells are modulated by the position and strength of the westerlies/easterlies, and the transition zone of the westerlies to easterlies (Figure 12a-c). This highlights how the change in upwelling, up the shelf break occurs and is consistent with the linear dynamics discussed in Section 2b, it also explains the discussed shelf temperature changes (Section 4b; Figure 6). Introducing a wall on the shelf (row 2 Figure 12), the overturning is similar to δ_{NONE} (row 1 Figure 12), except that the return flow on the shelf is no longer confined to the bottom Ekman layer but is higher up in the water column as a geostrophic return flow, this makes the anti-clockwise cell on the shelf more baroclinic. Despite there being no westward wind in Figure 12i-j, there is a weak, sub-surface anti-clockwise overturning cell on the shelf, this is likely a closure for the now opposing zonal flows (comparing Figure S2d-e,i-j) and the geostrophic return flow created by the gyre on the shelf. The deep ocean wall simulations δ_{owall} (row 3 Figure 12) are readily understood by considering the δ_{wail} case and the above arguments. Introducing a

full north-south wall (Figure 12r) leads to three gyres and their associated overturning (see Section 4a). As the winds are modified, e.g., with uniform westward wind (Figure 12p,q), the anti-clockwise cells above 1000m get larger and stronger. This is due to the increase in southward top Ekman transport at the southern boundary and the now southward top Ekman transport at the northern boundary. Similarly, with a uniform addition of eastward wind (Figure 12s,t), the near-surface clockwise-overturning cell gets larger and stronger. Revisiting Figure 6, but now with the control simulations removed (middle $c = 0$ column), Figure S1 shows that the zonally averaged temperature does change in a consistent, modest way with these overturning changes. The observed linking of the bottom and top overturning cells in Figure 12s-t, likely also explains the modest temperature changes seen in δ_{oowall} row 4 in Figure 8. In Sections 4a-d, we have considered large-scale time-mean circulation changes, in the remaining results sub-sections we examine the possible importance of eddy terms in the momentum (4e) and meridional advective heat (4f) balances.

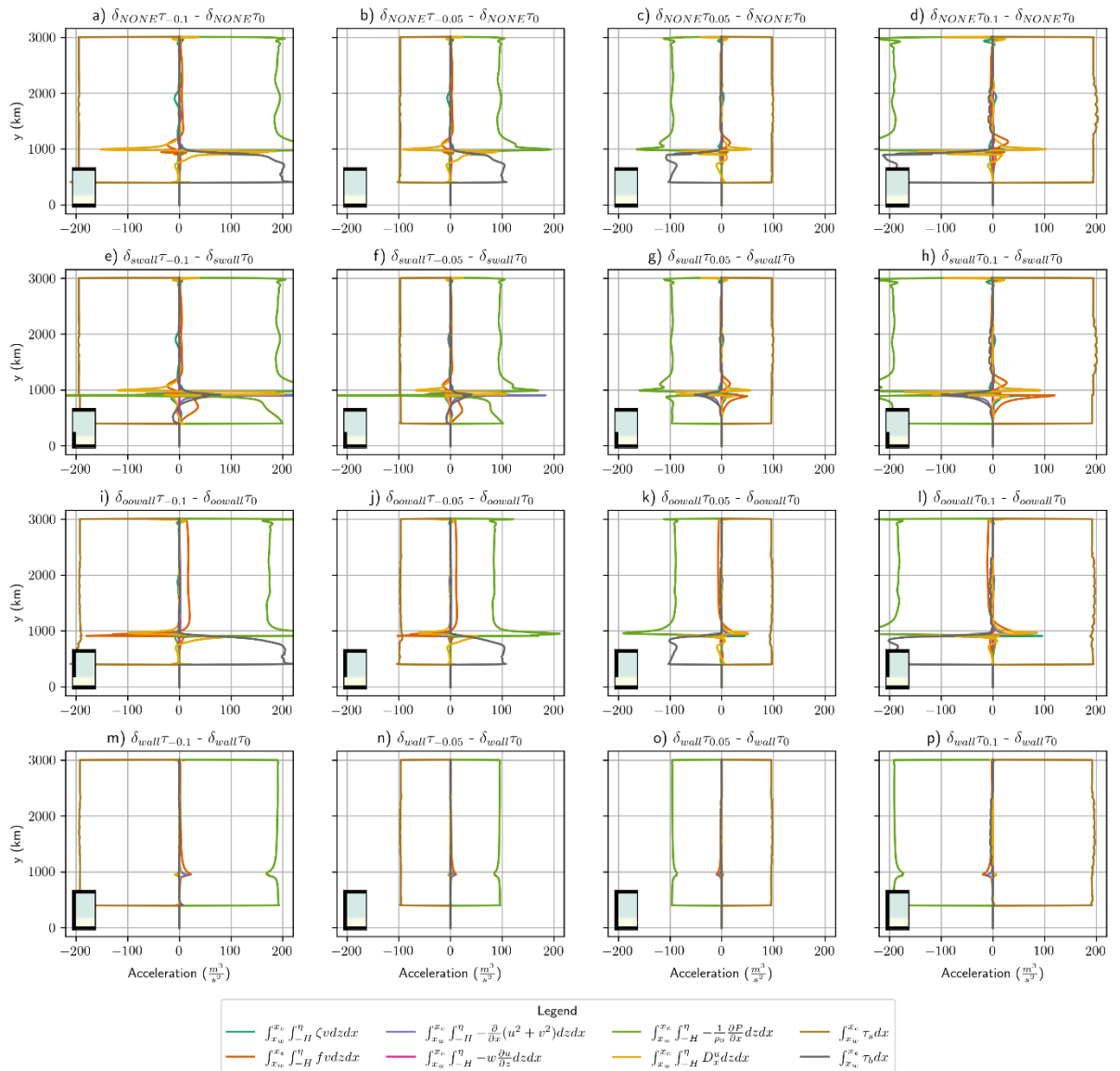
e Momentum budget

Several studies have found that eddies are a critical feature for fluxing heat and mass across the shelf break (Stern et al., 2015; Stewart & Thompson, 2015; St-Laurent et al., 2013). Throughout this study we have assumed that the changes in shelf temperatures are largely a result of momentum advection from circulation changes. Here, using depth and zonally integrated momentum budgets, we look to test whether these circulation changes are indeed linear (not related to eddies) and that the described geostrophic and Ekman dynamics (Section 2 and 4c) are what is driving those changes. The NEMO vector invariant form of the momentum equation is:

$$\frac{\partial \mathbf{u}_h}{\partial t} = - \left[(\nabla \times \mathbf{u}) \times \mathbf{u} + \frac{1}{2} \nabla u^2 \right]_h - f(k \times \mathbf{u})_h - \frac{1}{\rho_0} \nabla_h P + D^u + F^u$$

where f is the Coriolis parameter, \mathbf{u}_h is the horizontal velocity vector, ∇ and ∇_h is the 3D and 2D gradient operators, respectively. $[\cdot]_h$ is the horizontal component of a vector. F^u is the vertical divergence of the vertical diffusive momentum fluxes, i.e.

$\frac{\partial}{\partial z} (\kappa_z \frac{\partial \mathbf{u}_h}{\partial z})$ which includes the top and bottom stress where $\int_{-H}^{\eta} F^u dz = \tau_s - \tau_b$. D^u is the horizontal divergence of the horizontal diffusive momentum flux (i.e. $\nabla \cdot (\kappa_h \frac{\partial \mathbf{u}_h}{\partial x} + \kappa_h \frac{\partial \mathbf{u}_h}{\partial y})$), with the turbulent horizontal (κ_h) and vertical (κ_z) viscosities.



665

666

667

668

669

670

671

672

673

674

675

676

Figure 13. The 10 year time-average vertically and zonally integrated zonal momentum budget with anomalies from the control wind experiment shown. The terms are as described in Section 4e and indicated by the legend. Each row has a different boundary condition, in order: i) fully re-entrant, ii) blocked shelf, iii) blocked deep ocean and iv) fully blocked shelf and deep ocean, respectively. The small glyphs (bottom-left) schematically indicate the geometry under consideration in each panel.

Figure 13 shows the depth and zonally integrated x -momentum balance (Figure S3-S4 shows the raw values of both x and y budgets). Compared to Figure 7-12, Figure 13 has four columns instead of five, because we show momentum budget *anomalies* relative to the experiment with the control wind stress. As they are anomalies from the associated control experiment, Figure 13 (Figure S5) are primarily intended to be

compared along the rows. Under a change in wind forcing, over a long time-mean ($\frac{\partial \mathbf{u}_h}{\partial t} = 0$), Figure 13 highlights the importance of bottom friction and pressure gradients in balancing the input of momentum by the wind stress. In other words, unsurprisingly, the following terms dominate:

$$\int_{x_w}^{x_e} \tau_s dx = \underbrace{\int_{x_w}^{x_e} \tau_b dx}_{\text{throughflow}} + \underbrace{\int_{x_w}^{x_e} \int_{-H}^{\eta} \frac{\partial p}{\partial x} dz dx}_{\text{gyre}}$$

In regions where there is a throughflow regime and flat bottom (rows 1 and 3), the change in surface stress $\int_{x_w}^{x_e} \tau_s dx$ (light brown) is matched by a commensurate and opposite change in bottom stress $\int_{x_w}^{x_e} \tau_b dx$ (dark grey). In contrast, in regions where there is a gyre regime, consistent with previous studies (Munday et al., 2015; Olbers et al., 2007), the change in surface stress $\int_{x_w}^{x_e} \tau_s dx$ (light brown), is matched by a commensurate and opposite change in the depth and zonally integrated pressure gradient $\int_{x_w}^{x_e} \int_{-H}^{\eta} \frac{\partial p}{\partial x} dz dx$ (i.e. continental/topographic form stress). As the barotropic flow is blocked in the deep ocean, this balance between wind stress and topographic form stress exists in the deep ocean across all the rows. When the shelf and entire domain are blocked (rows 2 and 4) it additionally occurs on the shelf.

Figure S5 shows the depth and zonally integrated y-momentum balance, which highlights the importance of geostrophy. As expected, with changes in winds, we see minor changes in geostrophic balance in a fully blocked gyre regime (see discussion in Figure S5, Section 2b and 4c).

f Meridional advective Heat Transport

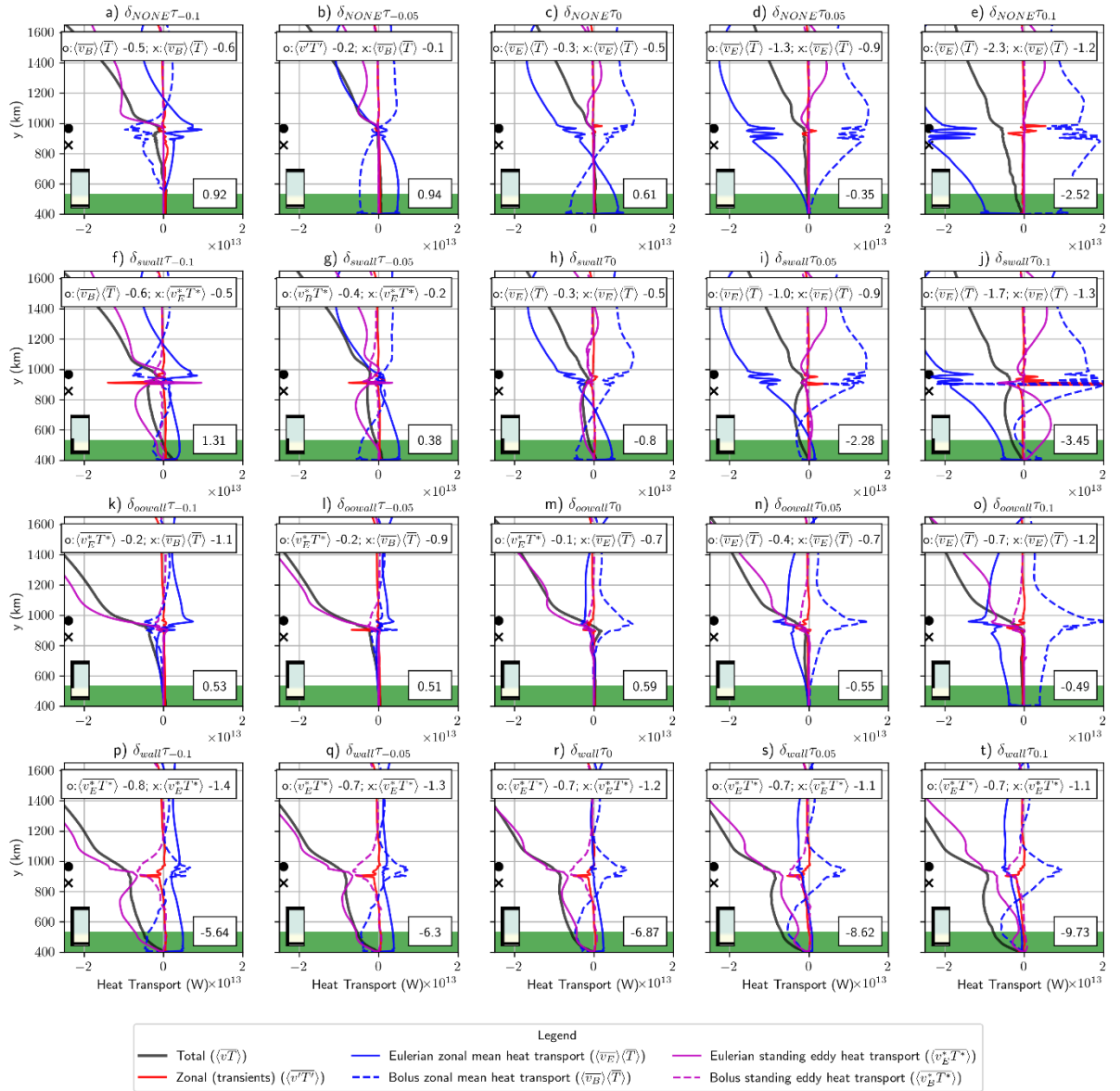


Figure 14. Same panel-experiment layout as Figure 7 but now the meridional heat transport for all experiments. The terms are as described in Eq. (1) in Section 4f and indicated by the legend. In each panel, the top inset gives the leading transport term and heat transport ($\times 10^{13}$) in two locations north and south of the shelf break in the open ocean (indicated by “•”) and shelf edge (indicated by “x”); the total is not considered. The bottom inset in each panel gives the total integrated heat transport ($\times 10^{13}$; black line), integrated over the shelf close to the imagined ice front (green shading). The small glyphs (bottom-left) schematically indicate the geometry under consideration in each panel.

In Section 4e, we found that nonlinear terms in the momentum budget were relatively unimportant (within the same geometries), that budget however, does not demonstrate that eddy advection is also negligible in the temperature equation. With this curiosity in mind, Figure 14 shows the following meridional advective heat balance:

$\rho_0 c_p L_x \int_{-H}^{\eta} \langle \overline{vT} \rangle dz = \rho_0 c_p L_x \int_{-H}^{\eta} \langle \overline{v_E} \rangle \langle \overline{T} \rangle dz + \rho_0 c_p L_x \int_{-H}^{\eta} \langle \overline{v_B} \rangle \langle \overline{T} \rangle dz +$ $\rho_0 c_p L_x \int_{-H}^{\eta} \langle \overline{v_E^* T^*} \rangle dz + \rho_0 c_p L_x \int_{-H}^{\eta} \langle \overline{v_B^* T^*} \rangle dz + \rho_0 c_p L_x \int_{-H}^{\eta} \langle \overline{v'T'} \rangle dz.$	(1)
--	-----

This balance is calculated using time-averages of the product of the meridional velocity (v), the temperature (T) and the vertical grid spacing at v -points ($e3v$) at every time step, this ensures temperature advection is properly accounted for (Munday et al., 2021). Here, as we are using GM to represent sub-gridscale mixing of tracers we have: $v = v_E + v_B$ which are the full, Eulerian and bolus velocities, respectively; the bolus velocity is what is due to GM. The remaining variables in the above equation are: $\rho_0 = 1026 \text{ kg/m}^3$ is the Boussinesq reference density, $c_p = 3991.9 \frac{\text{J}}{\text{kg K}}$ is the specific heat capacity, L_x is the zonal extent of the ocean, $-H$ is the depth of the sea bed and η is the height of the free surface. The operators used are: $\overline{\bullet}$ indicates a time average, \bullet' indicates the deviation from the time average, $\langle \bullet \rangle$ indicates a zonal average and \bullet^* indicates deviations from the zonal mean.

The first two terms on the right-hand side of Eq. (1) are the Eulerian ($\langle \overline{v_E} \rangle \langle \overline{T} \rangle$) and Bolus ($\langle \overline{v_B} \rangle \langle \overline{T} \rangle$) zonal mean heat transport, they largely reflect the overturning, and generally counteract one another (Figure S7). The next two terms in Eq. (1) are the Eulerian ($\langle \overline{v_E^* T^*} \rangle$) and Bolus ($\langle \overline{v_B^* T^*} \rangle$) heat transport from standing meanders, by construction, this includes any deviations from a strictly zonal flow. Finally, the last term ($\langle \overline{v'T'} \rangle$) in Eq. (1) is the total transient contribution. Thus, Figure 14 allows us to attribute differences in total heat transport to these processes. Supporting information Figures S6-S9 show spatial plots of these same terms.

The Figure 14 integrated heat transport near the ice front (bottom right inset) is consistent with the documented changes at the ice front as the winds change (Figure 8). Figure 8 shows warming when comparing within each boundary condition and Figure 14 corroborates this with the change in total advective heat transport. In more detail, for fully re-entrant, Figure 8b, 8c, 8d, 8e are increasingly warmer and the corresponding values in the inset in Figure 14 show increasingly stronger total southward heat transport. Similarly, for blocked shelf (f, g, h, i, j), blocked deep ocean (k, l, m colder than n, o) and full south-north block (p, q, r, s, t).

For heat transport across the shelf with a partially blocked western boundary (i.e. most simulations), Figure 14 shows that the most important term in the advective heat balance is the Eulerian zonal mean heat transport ($\langle \overline{v_E} \rangle \langle \overline{T} \rangle$), particularly for simulations with control or

positive offset winds (Figure 14c, d, e, h, i, j, m, n, o). Since this term represents the overturning circulation, it is unsurprising that the plan view plot of this term (Figure S7) shows changes that are consistent with the changes in Ekman overturning cells discussed earlier (Section 2b and 4 earlier). In most of the remaining cases with an unblocked western boundary (Figure 14a, b, k, l), under negative offset winds, the Bolus term ($\langle \overline{v_B} \rangle \langle \overline{T} \rangle$) becomes important. Interestingly, Figure 14b, f, g, k, l, m top inset, shows that the leading term that transports heat towards the ice front can be different south and north of the shelf break. In the case of a fully blocked western boundary (bottom row Figure 14), south of the shelf break, the Eulerian ($\langle \overline{v_E^*} \overline{T^*} \rangle$) heat transport from standing meanders is the most important term. In terms of the modest temperature changes in a fully blocked regime under a change in winds (bottom row Figure 8), the modest warming is due to large-scale increases in southward heat transport from $\langle \overline{v_E} \rangle \langle \overline{T} \rangle$ and localized shelf changes in $\langle \overline{v'T'} \rangle$ (bottom rows Figure 14, S7 top set and S9).

5 Summary and Discussion

In this study, we have explored how basin geometry and wind shifts have a large role in determining the temperature structure on Antarctica's shelf seas. Furthermore, the basin geometry influences how susceptible the shelf temperatures are to changes in winds.

We have used a simple barotropic model (Stommel's planetary geostrophic equations in Section 2), to explore the linear dynamical balances that change when the circulation regime changes from a channel to a gyre, we also examined how the Ekman and geostrophic circulations respond to changes in surface forcing within these two regimes, all in the absence of baroclinicity and topography. We then used the primitive equation ocean model NEMO (Section 4) with varying temperature to see if the barotropic arguments from Section 2 could explain the more complex circulation changes (Section 4c). Despite the NEMO model configuration used here including complications such as bathymetry and baroclinicity, we find that the time-mean results are largely understood by the simple barotropic model. Fundamentally, the time-mean equilibrated differences between the geometries and winds, can be understood by changes in the Ekman layers and a geostrophic circulation compensating for changes in boundary conditions as a response to a fixed Ekman layer transport (Section 2b-c and 4c). Specifically, irrespective of boundary condition, the westerly

and easterly stresses create a near surface northward and southward transport in the top Ekman layer, respectively. As we discuss in Section 2 and Section 4, the interior responds to these transports where the boundary condition determines how the response is constrained. In brief, we summarise the response as follows. In the case of a throughflow, as the easterly-westerly wind transition moves south, so does the confluence region in the bottom layers, and critically, the upwelling region that brings warm waters onto the shelf (Section 2b). We note that these results are consistent with more realistic simulations in the Amundsen Sea (Caillet et al., 2023; Haigh et al., 2023). In a gyre regime, when a wall is introduced, the return flow is no longer confined to the frictionally balanced bottom Ekman layers but rather a wall creates topographic form stress enabling a geostrophic return flow at every depth where the wall is present. We noted that the introduction of a deep ocean wall (Figure 7) led to the flattening of isotherms in the deep ocean, with less warm waters close to the shelf. Applying the above arguments, we see this is because the return flow set up by the near-surface Ekman transport is more evenly distributed throughout the water column than when the return flow is in the frictionally balanced bottom Ekman layer. Whilst these largely linear dynamics balance have been understood for some time (e.g. Veronis (1996) and Vallis (2017)), we think this is the first time they have been re-visited in terms of Antarctic shelf temperatures, with combinations of circulation regimes, in a realistic primitive equation ocean model.

When it comes to understanding future Southern Ocean projections, from the gyre regime simulations with a constant offset in the winds, we think this work demonstrates that we need to diagnose how the winds change, i.e. strength, a latitudinal shift, a change in curl as this allows us to manage our expectations for the change we expect. Despite several studies focused on eddies as a critical feature for fluxing heat and mass across the shelf break (Stern et al., 2015; Stewart & Thompson, 2015; St-Laurent et al., 2013), in this instance, NEMO's momentum and heat budget show that over equilibrated timescales, the system response to *surface forcing changes* is first-order linear (some geometry changes, e.g., Figure 7c,h and S4c,h involve non-linear advection). The linear nature of the surface forcing response may be because of the focus on equilibrated changes. Furthermore, while these simulations lack many important features (e.g., buoyancy forcing changes, varying forcing, sea ice, ice shelves, meridional winds, realistic bathymetry et cetera) we hope this study encourages

others to consider basin geometry and easterlies in related idealized studies; our own work is ongoing in adding other features.

A remaining question is how the simplest of geometries and forcing considered here is relevant to the real ocean. To manage expectations, as winds change, we need metrics to diagnose when we are in a gyre or throughflow regime, blocked f/h contours offer some barotropic insight here but the mechanisms described in this paper apply in partial cases too. In this study, we intentionally made the transitions distinct, making the diagnostics simple (Section 4d) but in the real Southern Ocean the dynamics is more mixed. Indeed, Masich et al. (2015) found that 95% of the momentum input by the wind at ACC latitudes is balanced by topographic form stress. We thus need a stratification dependent metric to diagnose the degree to which a region is in a channel or gyre regime. We think work such as Figure 5 from *Waldman and Giordani* (2022) diagnosing the dominant vorticity balance in different regions is work in the right direction. We assume this kind of diagnostic would need to reconcile throughflow and gyre dynamics into a singular framework, considerable discussion has occurred on this topic (Hughes, 2000, 2002; Hughes & Cuevas, 2001; Jackson et al., 2006; Olbers, 1998; Olbers et al., 2004; Warren et al., 1996). On applying Sverdrup theory in the Southern Ocean, *Hughes* (2002) used Sverdrup like theories from (Stommel, 1957; Webb, 1993) to estimate ACC transport, see (LaCasce & Isachsen, 2010) for a more general review of linear theories. For vorticity in gyres alone, direct buoyancy forcing aside, the dominant terms are still debated. For example, *Hughes* (2000) notes that the historical tendency to focus on gyres in boxes with straight walls (Walter H. Munk, 1950; Stommel, 1948) has led to the view that the return flow in western boundary currents occurs due to friction and viscosity. In reality, coastlines are sloped, leading to inviscid western currents where, like the channel regime, the wind stress is balanced by topographic form stress, or in vorticity parlance bottom pressure “torques” balance the wind stress curl (e.g. Schoonover et al., 2017; Styles et al., 2021). Here, we are interested in heat transport across Antarctica’s shelf break, if we think of this in terms of momentum transport across f/h contours then the above theories highlight (for vorticity), that momentum transport across a sloping shelf break or bottom ridge requires an additional source of vorticity, and the kind of dissipation (e.g. Munk, Stommel et cetera) changes depending on the nature of the feature. If we are to understand

how Antarctica's shelf temperatures will respond to a warming climate, then further work is needed on how to apply these ideas across mixed flow regimes.

Acknowledgments.

This work used the ARCHER2 UK National Supercomputing Service (<https://www.archer2.ac.uk>). Figure 1a was created using ETOPO1 (NOAA National Geophysical Data Center, 2009). C.B. and A. J. are supported by the European Union's Horizon 2020 research and innovation programme under grant agreement no. 820575 (TiPACCs). For the purpose of Open Access, the author has applied a CC BY public copyright licence to any Author Accepted Manuscript (AAM) version arising from this submission. C.B. gratefully acknowledges Paul Holland for asking *the* question and Andrew Kiss for a 2014 lecture on western boundary currents, the start of the journey. We thank Dave Storkey for his work on the momentum trend budgets (branch below).

Data Availability Statement.

Key NEMO configuration files and model outputs will be made available on Zenodo following final revisions of this article. The NEMO configuration used in this article uses NEMO version 4.0.4 with the following branch: branches/UKMO/NEMO_4.0.4_momentum_trends @ 15194. This branch can be found on the (old svn) repository at: <https://forge.ipsl.jussieu.fr/nemo/browser/NEMO/>. The finite element method solve for Stommel's planetary geostrophic equations in Section 2 used Mathematica v13.2.

REFERENCES

- Abernathey, R., Marshall, J., & Ferreira, D. (2011). The Dependence of Southern Ocean Meridional Overturning on Wind Stress. *Journal of Physical Oceanography*, 41(12).
<https://doi.org/10.1175/JPO-D-11-023.1>
- Allison, L., Johnson, H., & Marshall, D. (2011). Spin-up and adjustment of the Antarctic Circumpolar Current and global pycnocline. *Journal of Marine Research*, 69(2).
Retrieved from https://elischolar.library.yale.edu/journal_of_marine_research/300

858 Armitage, T. W. K., Kwok, R., Thompson, A. F., & Cunningham, G. (2018). Dynamic
859 Topography and Sea Level Anomalies of the Southern Ocean: Variability and
860 Teleconnections. *Journal of Geophysical Research: Oceans*, 123(1), 613–630.
861 <https://doi.org/10.1002/2017JC013534>

862 Boyer, Tim P., García, Hernán E., Locarnini, Ricardo A., Zweng, Melissa M., Mishonov,
863 Alexey V., Reagan, James R., et al. (2018). World Ocean Atlas 2018 [Data set].
864 Dataset., NOAA National Centers for Environmental Information. Retrieved from
865 [https://www.ncei.noaa.gov/access/metadata/landing-](https://www.ncei.noaa.gov/access/metadata/landing-page/bin/iso?id=gov.noaa.nodc:NCEI-WOA18)
866 [page/bin/iso?id=gov.noaa.nodc:NCEI-WOA18](https://www.ncei.noaa.gov/access/metadata/landing-page/bin/iso?id=gov.noaa.nodc:NCEI-WOA18)

867 Bracegirdle, T. J., Shuckburgh, E., Sallee, J.-B., Wang, Z., Meijers, A. J. S., Bruneau, N., et
868 al. (2013). Assessment of surface winds over the Atlantic, Indian, and Pacific Ocean
869 sectors of the Southern Ocean in CMIP5 models: historical bias, forcing response, and
870 state dependence: CMIP5 SOUTHERN OCEAN SURFACE WINDS. *Journal of*
871 *Geophysical Research: Atmospheres*, 118(2), 547–562.
872 <https://doi.org/10.1002/jgrd.50153>

873 Bryan, K. (1963). A Numerical Investigation of a Nonlinear Model of a Wind-Driven Ocean.
874 *Journal of the Atmospheric Sciences*, 20(6), 594–606. [https://doi.org/10.1175/1520-](https://doi.org/10.1175/1520-0469(1963)020<0594:ANIOAN>2.0.CO;2)
875 [0469\(1963\)020<0594:ANIOAN>2.0.CO;2](https://doi.org/10.1175/1520-0469(1963)020<0594:ANIOAN>2.0.CO;2)

876 Caillet, J., Jourdain, N. C., Mathiot, P., Hellmer, H. H., & Mouginot, J. (2023). Drivers and
877 Reversibility of Abrupt Ocean State Transitions in the Amundsen Sea, Antarctica.
878 *Journal of Geophysical Research: Oceans*, 128(1), e2022JC018929.
879 <https://doi.org/10.1029/2022JC018929>

880 Constantinou, N. C., & Hogg, A. McC. (2019). Eddy Saturation of the Southern Ocean: A
881 Baroclinic Versus Barotropic Perspective. *Geophysical Research Letters*, 46(21),
882 12202–12212. <https://doi.org/10.1029/2019GL084117>

883 Donohue, K. A., Tracey, K. L., Watts, D. R., Chidichimo, M. P., & Chereskin, T. K. (2016).
884 Mean Antarctic Circumpolar Current transport measured in Drake Passage.
885 *Geophysical Research Letters*, 43(22), 11,760–11,767.
886 <https://doi.org/10.1002/2016GL070319>

887 Dotto, T. S., Naveira Garabato, A., Bacon, S., Tsamados, M., Holland, P. R., Hooley, J., et al.
888 (2018). Variability of the Ross Gyre, Southern Ocean: Drivers and Responses
889 Revealed by Satellite Altimetry. *Geophysical Research Letters*.
890 <https://doi.org/10.1029/2018GL078607>

891 Farneti, R., Downes, S. M., Griffies, S. M., Marsland, S. J., Behrens, E., Bentsen, M., et al.
892 (2015). An assessment of Antarctic Circumpolar Current and Southern Ocean
893 meridional overturning circulation during 1958–2007 in a suite of interannual CORE-
894 II simulations. *Ocean Modelling*, 93, 84–120.
895 <https://doi.org/10.1016/j.ocemod.2015.07.009>

896 Gent, P. R., & McWilliams, J. C. (1990). Isopycnal Mixing in Ocean Circulation Models.
897 *Journal of Physical Oceanography*, 20(1), 150–155. [https://doi.org/10.1175/1520-](https://doi.org/10.1175/1520-0485(1990)020<0150:IMIOCM>2.0.CO;2)
898 [0485\(1990\)020<0150:IMIOCM>2.0.CO;2](https://doi.org/10.1175/1520-0485(1990)020<0150:IMIOCM>2.0.CO;2)

899 Gent, P. R., Willebrand, J., McDougall, T. J., & McWilliams, J. C. (1995). Parameterizing
900 Eddy-Induced Tracer Transports in Ocean Circulation Models. *Journal of Physical*
901 *Oceanography*, 25(4), 463–474. [https://doi.org/10.1175/1520-](https://doi.org/10.1175/1520-0485(1995)025<0463:PEITTI>2.0.CO;2)
902 [0485\(1995\)025<0463:PEITTI>2.0.CO;2](https://doi.org/10.1175/1520-0485(1995)025<0463:PEITTI>2.0.CO;2)

- 903 Gnanadesikan, A., & Hallberg, R. W. (2000). On the Relationship of the Circumpolar Current
904 to Southern Hemisphere Winds in Coarse-Resolution Ocean Models. *Journal of*
905 *Physical Oceanography, Volume 30*(Issue 8). Retrieved from
906 [https://journals.ametsoc.org/view/journals/phoc/30/8/1520-](https://journals.ametsoc.org/view/journals/phoc/30/8/1520-0485_2000_030_2013_otrotc_2.0.co_2.xml)
907 [0485_2000_030_2013_otrotc_2.0.co_2.xml](https://journals.ametsoc.org/view/journals/phoc/30/8/1520-0485_2000_030_2013_otrotc_2.0.co_2.xml)
- 908 Gómez-Valdivia, F., Holland, P. R., Siahaan, A., Dutrieux, P., & Young, E. (2023). Projected
909 West Antarctic Ocean Warming Caused by an Expansion of the Ross Gyre.
910 *Geophysical Research Letters, 50*(6), e2023GL102978.
911 <https://doi.org/10.1029/2023GL102978>
- 912 Goyal, R., Sen Gupta, A., Jucker, M., & England, M. H. (2021). Historical and Projected
913 Changes in the Southern Hemisphere Surface Westerlies. *Geophysical Research*
914 *Letters, 48*(4), e2020GL090849. <https://doi.org/10.1029/2020GL090849>
- 915 Gray, A. R., & Riser, S. C. (2014). A Global Analysis of Sverdrup Balance Using Absolute
916 Geostrophic Velocities from Argo. *Journal of Physical Oceanography, 44*(4), 1213–
917 1229. <https://doi.org/10.1175/JPO-D-12-0206.1>
- 918 Haigh, M., Holland, P. R., & Jenkins, A. (2023). The Influence of Bathymetry Over Heat
919 Transport Onto the Amundsen Sea Continental Shelf. *Journal of Geophysical*
920 *Research: Oceans, 128*(5), e2022JC019460. <https://doi.org/10.1029/2022JC019460>
- 921 Hattermann, T. (2018). Antarctic Thermocline Dynamics along a Narrow Shelf with Easterly
922 Winds. *Journal of Physical Oceanography, 48*(10), 2419–2443.
923 <https://doi.org/10.1175/JPO-D-18-0064.1>
- 924 Hidaka, K., & Tsuchiya, M. (1953). On the Antarctic circumpolar current. *Journal of Marine*
925 *Research, 12*(2). Retrieved from
926 https://elischolar.library.yale.edu/journal_of_marine_research/794

- 927 Hogg, A. McC., & Gayen, B. (2020). Ocean Gyres Driven by Surface Buoyancy Forcing.
928 *Geophysical Research Letters*, 47(16), e2020GL088539.
929 <https://doi.org/10.1029/2020GL088539>
- 930 Hughes, C. W. (1997). Comments on “On the Obscurantist Physics of ‘Form Drag’ in
931 Theorizing about the Circumpolar Current.” *Journal of Physical Oceanography*,
932 27(1), 209–210. [https://doi.org/10.1175/1520-](https://doi.org/10.1175/1520-0485(1997)027<0209:COOTOP>2.0.CO;2)
933 0485(1997)027<0209:COOTOP>2.0.CO;2
- 934 Hughes, C. W. (2000). A theoretical reason to expect inviscid western boundary currents in
935 realistic oceans. *Ocean Modelling*, 2(1), 73–83. [https://doi.org/10.1016/S1463-](https://doi.org/10.1016/S1463-5003(00)00011-1)
936 5003(00)00011-1
- 937 Hughes, C. W. (2002). Sverdrup-like theories of the Antarctic Circumpolar Current. *Journal*
938 *of Marine Research*, 60(1), 1–17. <https://doi.org/10.1357/002224002762341221>
- 939 Hughes, C. W., & Cuevas, B. A. de. (2001). Why Western Boundary Currents in Realistic
940 Oceans are Inviscid: A Link between Form Stress and Bottom Pressure Torques.
941 *Journal of Physical Oceanography*, 31(10), 2871–2885. [https://doi.org/10.1175/1520-](https://doi.org/10.1175/1520-0485(2001)031<2871:WWBCIR>2.0.CO;2)
942 0485(2001)031<2871:WWBCIR>2.0.CO;2
- 943 Jackson, L., Hughes, C. W., & Williams, R. G. (2006). Topographic Control of Basin and
944 Channel Flows: The Role of Bottom Pressure Torques and Friction. *Journal of*
945 *Physical Oceanography*, 36(9), 1786–1805. <https://doi.org/10.1175/JPO2936.1>
- 946 Karnauskas, K. (2020). *Physical Oceanography and Climate*. Cambridge University Press.
947 <https://doi.org/10.1017/9781108529594>
- 948 LaCasce, J. H., & Isachsen, P. E. (2010). The linear models of the ACC. *Progress in*
949 *Oceanography*, 84(3), 139–157. <https://doi.org/10.1016/j.pocean.2009.11.002>

950 Masich, J., Chereskin, T. K., & Mazloff, M. R. (2015). Topographic form stress in the
 951 Southern Ocean State Estimate. *Journal of Geophysical Research: Oceans*, 120(12),
 952 7919–7933. <https://doi.org/10.1002/2015JC011143>
 953 McWilliams, J. C. (2011). Fundamentals of Geophysical Fluid Dynamics, 284.
 954 Meredith, M. P., Woodworth, P. L., Chereskin, T. K., Marshall, D. P., Allison, L. C., Bigg,
 955 G. R., et al. (2011). Sustained Monitoring of the Southern Ocean at Drake Passage:
 956 Past Achievements and Future Priorities. *Reviews of Geophysics*, 49(4).
 957 <https://doi.org/10.1029/2010RG000348>
 958 Morrison, A. K., Hogg, A. M., & Ward, M. L. (2011). Sensitivity of the Southern Ocean
 959 overturning circulation to surface buoyancy forcing: SOUTHERN OCEAN
 960 OVERTURNING. *Geophysical Research Letters*, 38(14), n/a-n/a.
 961 <https://doi.org/10.1029/2011GL048031>
 962 Munday, D. R., Johnson, H. L., & Marshall, D. P. (2015). The role of ocean gateways in the
 963 dynamics and sensitivity to wind stress of the early Antarctic Circumpolar Current.
 964 *Paleoceanography*, 30(3), 284–302. <https://doi.org/10.1002/2014PA002675>
 965 Munday, David R., Johnson, H. L., & Marshall, D. P. (2013). Eddy Saturation of Equilibrated
 966 Circumpolar Currents. *Journal of Physical Oceanography*, 43(3), 507–532.
 967 <https://doi.org/10.1175/JPO-D-12-095.1>
 968 Munday, David R., Zhai, X., Harle, J., Coward, A. C., & Nurser, A. J. G. (2021). Relative vs.
 969 absolute wind stress in a circumpolar model of the Southern Ocean. *Ocean Modelling*,
 970 168, 101891. <https://doi.org/10.1016/j.ocemod.2021.101891>
 971 Munk, W H, & Palmen, E. (1951). Note on the Dynamics of the Antarctic Circumpolar
 972 Current, 3.

- 973 Munk, Walter H. (1950). On the wind-driven ocean circulation. *Journal of Meteorology*.
 974 [https://doi.org/10.1175/1520-0469\(1950\)007<0080:OTWDOC>2.0.CO;2](https://doi.org/10.1175/1520-0469(1950)007<0080:OTWDOC>2.0.CO;2)
- 975 Neme, J., England, M. H., & Hogg, A. McC. (2021). Seasonal and Interannual Variability of
 976 the Weddell Gyre From a High-Resolution Global Ocean-Sea Ice Simulation During
 977 1958–2018. *Journal of Geophysical Research: Oceans*, 126(11), e2021JC017662.
 978 <https://doi.org/10.1029/2021JC017662>
- 979 NOAA National Geophysical Data Center. (2009). ETOPO1 1 Arc-Minute Global Relief
 980 Model [Data set]. NOAA National Centers for Environmental Information. Retrieved
 981 from [https://www.ncei.noaa.gov/access/metadata/landing-](https://www.ncei.noaa.gov/access/metadata/landing-page/bin/iso?id=gov.noaa.ngdc.mgg.dem:316)
 982 [page/bin/iso?id=gov.noaa.ngdc.mgg.dem:316](https://www.ncei.noaa.gov/access/metadata/landing-page/bin/iso?id=gov.noaa.ngdc.mgg.dem:316)
- 983 Olbers, D. (1998). Comments on “On the Obscurantist Physics of ‘Form Drag’ in Theorizing
 984 about the Circumpolar Current. *Journal of Physical Oceanography*, 28(8), 1647–
 985 1654. [https://doi.org/10.1175/1520-0485\(1998\)028<1647:COOTOP>2.0.CO;2](https://doi.org/10.1175/1520-0485(1998)028<1647:COOTOP>2.0.CO;2)
- 986 Olbers, D., Borowski, D., Völker, C., & Wölff, J.-O. (2004). The dynamical balance,
 987 transport and circulation of the Antarctic Circumpolar Current. *Antarctic Science*,
 988 16(4), 439–470. <https://doi.org/10.1017/S0954102004002251>
- 989 Olbers, D., Lettmann, K., & Timmermann, R. (2007). Six circumpolar currents—on the
 990 forcing of the Antarctic Circumpolar Current by wind and mixing. *Ocean Dynamics*,
 991 57(1), 12–31. <https://doi.org/10.1007/s10236-006-0087-9>
- 992 Olbers, D., Willebrand, J., & Eden, C. (2012). *Ocean Dynamics*. Berlin, Heidelberg: Springer
 993 Berlin Heidelberg. <https://doi.org/10.1007/978-3-642-23450-7>
- 994 Park, Y.-H., Park, T., Kim, T.-W., Lee, S.-H., Hong, C.-S., Lee, J.-H., et al. (2019).
 995 Observations of the Antarctic Circumpolar Current Over the Udintsev Fracture Zone,

996 the Narrowest Choke Point in the Southern Ocean. *Journal of Geophysical Research:*
 997 *Oceans*, 124(7), 4511–4528. <https://doi.org/10.1029/2019JC015024>
 998 Patmore, R. D., Holland, P. R., Munday, D. R., Naveira Garabato, A. C., Stevens, D. P., &
 999 Meredith, M. P. (2019). Topographic Control of Southern Ocean Gyres and the
 1000 Antarctic Circumpolar Current: A Barotropic Perspective. *Journal of Physical*
 1001 *Oceanography*, 49(12), 3221–3244. <https://doi.org/10.1175/JPO-D-19-0083.1>
 1002 Pauthenet, E., Sallée, J.-B., Schmidtko, S., & Nerini, D. (2021). Seasonal Variation of the
 1003 Antarctic Slope Front Occurrence and Position Estimated from an Interpolated
 1004 Hydrographic Climatology. *Journal of Physical Oceanography*, 51(5), 1539–1557.
 1005 <https://doi.org/10.1175/JPO-D-20-0186.1>
 1006 Pedlosky, J. (1996). *Ocean Circulation Theory*. Berlin, Heidelberg: Springer Berlin
 1007 Heidelberg. <https://doi.org/10.1007/978-3-662-03204-6>
 1008 Pritchard, H. D., Ligtenberg, S. R. M., Fricker, H. A., Vaughan, D. G., van den Broeke, M.
 1009 R., & Padman, L. (2012). Antarctic ice-sheet loss driven by basal melting of ice
 1010 shelves. *Nature*, 484(7395), 502–505. <https://doi.org/10.1038/nature10968>
 1011 Purich, A., & England, M. H. (2021). Historical and Future Projected Warming of Antarctic
 1012 Shelf Bottom Water in CMIP6 Models. *Geophysical Research Letters*, 48(10).
 1013 <https://doi.org/10.1029/2021GL092752>
 1014 Schoonover, J., Dewar, W. K., Wienders, N., & Deremble, B. (2017). Local Sensitivities of
 1015 the Gulf Stream Separation. *Journal of Physical Oceanography*, 47(2), 353–373.
 1016 <https://doi.org/10.1175/JPO-D-16-0195.1>
 1017 Spence, P., Griffies, S. M., England, M. H., Hogg, A. McC., Saenko, O. A., & Jourdain, N.
 1018 C. (2014). Rapid subsurface warming and circulation changes of Antarctic coastal

1019 waters by poleward shifting winds: Antarctic subsurface ocean warming. *Geophysical*
 1020 *Research Letters*, 41(13), 4601–4610. <https://doi.org/10.1002/2014GL060613>

1021 Spence, P., Holmes, R. M., Hogg, A. McC., Griffies, S. M., Stewart, K. D., & England, M. H.
 1022 (2017). Localized rapid warming of West Antarctic subsurface waters by remote
 1023 winds. *Nature Climate Change*, 7(8), 595–603. <https://doi.org/10.1038/nclimate3335>

1024 Stern, A., Nadeau, L.-P., & Holland, D. (2015). Instability and Mixing of Zonal Jets along an
 1025 Idealized Continental Shelf Break. *American Meteorological Society*. Retrieved from
 1026 <https://dspace.mit.edu/handle/1721.1/102085>

1027 Stewart, A. L. (2021). Warming spins up the Southern Ocean. *Nature Climate Change*, 1–2.
 1028 <https://doi.org/10.1038/s41558-021-01227-y>

1029 Stewart, A. L., & Thompson, A. F. (2012). Sensitivity of the ocean’s deep overturning
 1030 circulation to easterly Antarctic winds. *Geophysical Research Letters*, 39(18).
 1031 <https://doi.org/10.1029/2012GL053099>

1032 Stewart, A. L., & Thompson, A. F. (2015). Eddy-mediated transport of warm Circumpolar
 1033 Deep Water across the Antarctic Shelf Break. *Geophysical Research Letters*, 42(2),
 1034 432–440. <https://doi.org/10.1002/2014GL062281>

1035 Stewart, A. L., McWilliams, J. C., & Solodoch, A. (2021). On the Role of Bottom Pressure
 1036 Torques in Wind-Driven Gyres. *Journal of Physical Oceanography*, 51(5), 1441–
 1037 1464. <https://doi.org/10.1175/JPO-D-20-0147.1>

1038 St-Laurent, P., Klinck, J. M., & Dinniman, M. S. (2013). On the Role of Coastal Troughs in
 1039 the Circulation of Warm Circumpolar Deep Water on Antarctic Shelves. *Journal of*
 1040 *Physical Oceanography*, 43(1), 51–64. <https://doi.org/10.1175/JPO-D-11-0237.1>

- 1041 Stommel, H. (1948). The westward intensification of wind-driven ocean currents.
 1042 *Transactions, American Geophysical Union*, 29(2), 202.
 1043 <https://doi.org/10.1029/TR029i002p00202>
- 1044 Stommel, H. (1957). A survey of ocean current theory. *Deep Sea Research (1953)*, 4, 149–
 1045 184. [https://doi.org/10.1016/0146-6313\(56\)90048-X](https://doi.org/10.1016/0146-6313(56)90048-X)
- 1046 Straub, D. N. (1993). On the Transport and Angular Momentum Balance of Channel Models
 1047 of the Antarctic Circumpolar Current. *Journal of Physical Oceanography*, 23(4), 776–
 1048 782. [https://doi.org/10.1175/1520-0485\(1993\)023<0776:OTTAAM>2.0.CO;2](https://doi.org/10.1175/1520-0485(1993)023<0776:OTTAAM>2.0.CO;2)
- 1049 Styles, A., Bell, M., Marshall, D., & Storkey, D. (2021, October 28). Spurious forces can
 1050 dominate the vorticity budget of ocean gyres on the C-grid [preprint].
 1051 <https://doi.org/10.1002/essoar.10508527.1>
- 1052 Tansley, C. E., & Marshall, D. P. (2001). On the Dynamics of Wind-Driven Circumpolar
 1053 Currents. *Journal of Physical Oceanography*, 31(11), 3258–3273.
 1054 [https://doi.org/10.1175/1520-0485\(2001\)031<3258:OTDOWD>2.0.CO;2](https://doi.org/10.1175/1520-0485(2001)031<3258:OTDOWD>2.0.CO;2)
- 1055 Thompson, A. F., Stewart, A. L., Spence, P., & Heywood, K. J. (2018). The Antarctic Slope
 1056 Current in a Changing Climate. *Reviews of Geophysics*, 56(4), 741–770.
 1057 <https://doi.org/10.1029/2018RG000624>
- 1058 Tsujino, H., Urakawa, S., Nakano, H., Small, R. J., Kim, W. M., Yeager, S. G., et al. (2018).
 1059 JRA-55 based surface dataset for driving ocean–sea-ice models (JRA55-do). *Ocean*
 1060 *Modelling*, 130, 79–139. <https://doi.org/10.1016/j.ocemod.2018.07.002>
- 1061 Vallis, G. K. (2017). *Atmospheric and Oceanic Fluid Dynamics: Fundamentals and Large-*
 1062 *Scale Circulation* (2nd ed.). Cambridge: Cambridge University Press.
 1063 <https://doi.org/10.1017/9781107588417>

1064 Verfaillie, D., Pelletier, C., Goosse, H., Jourdain, N. C., Bull, C. Y. S., Dalaiden, Q., et al.
 1065 (2022). The circum-Antarctic ice-shelves respond to a more positive Southern
 1066 Annular Mode with regionally varied melting. *Communications Earth &*
 1067 *Environment*, 3(1), 1–12. <https://doi.org/10.1038/s43247-022-00458-x>
 1068 Veronis, G. (1996). Effect of a Constant, Zonal Wind on Wind-Driven Ocean Circulation.
 1069 *Journal of Physical Oceanography*, 26(11), 2525–2528. [https://doi.org/10.1175/1520-](https://doi.org/10.1175/1520-0485(1996)026<2525:EOACZW>2.0.CO;2)
 1070 0485(1996)026<2525:EOACZW>2.0.CO;2
 1071 Visbeck, M., Marshall, J., Haine, T., & Spall, M. (1997). Specification of Eddy Transfer
 1072 Coefficients in Coarse-Resolution Ocean Circulation Models. *Journal of Physical*
 1073 *Oceanography*, 27(3), 381–402. [https://doi.org/10.1175/1520-](https://doi.org/10.1175/1520-0485(1997)027<0381:SOETCI>2.0.CO;2)
 1074 0485(1997)027<0381:SOETCI>2.0.CO;2
 1075 Waldman, R., & Giordani, H. (2022). Ocean barotropic vorticity balances: theory and
 1076 application to numerical models, *Authorea*. <https://doi.org/10.1002/essoar.10511808.1>
 1077 Waldman, R., & Giordani, H. (2023). Ocean Barotropic Vorticity Balances: Theory and
 1078 Application to Numerical Models. *Journal of Advances in Modeling Earth Systems*,
 1079 15(4), e2022MS003276. <https://doi.org/10.1029/2022MS003276>
 1080 Warren, B. A., LaCasce, J. H., & Robbins, P. E. (1996). On the Obscurantist Physics of
 1081 “Form Drag” in Theorizing about the Circumpolar Current. *Journal of Physical*
 1082 *Oceanography*, 26(10), 2297–2301. [https://doi.org/10.1175/1520-](https://doi.org/10.1175/1520-0485(1996)026<2297:OTOPOD>2.0.CO;2)
 1083 0485(1996)026<2297:OTOPOD>2.0.CO;2
 1084 Webb, D. J. (1993). A simple model of the effect of the Kerguelen Plateau on the strength of
 1085 the Antarctic Circumpolar Current. *Geophysical & Astrophysical Fluid Dynamics*,
 1086 70(1–4), 57–84. <https://doi.org/10.1080/03091929308203587>

- 1087 Whitworth, T., Orsi, A. H., Kim, S.-., Nowlin, W. D., & Locarnini, R. A. (1998). Water
1088 masses and mixing near the Antarctic Slope Front. In S. S. Jacobs & R. F. Weiss
1089 (Eds.), *Ocean, ice, and atmosphere: interactions at the Antarctic continental margin*
1090 (Vol. 75, pp. 1–27). American Geophysical Union.
- 1091 Wilson, E. A., Thompson, A. F., Stewart, A. L., & Sun, S. (2022). Bathymetric control of
1092 subpolar gyres and the overturning circulation in the Southern Ocean. *Journal of*
1093 *Physical Oceanography*, 1(aop). <https://doi.org/10.1175/JPO-D-21-0136.1>
- 1094 Zhai, X., & Munday, D. R. (2014). Sensitivity of Southern Ocean overturning to wind stress
1095 changes: Role of surface restoring time scales. *Ocean Modelling*, 84, 12–25.
1096 <https://doi.org/10.1016/j.ocemod.2014.09.004>
- 1097

Supplementary material

Influence of topography and winds on the distribution of water masses on the Antarctic Continental Shelf

Christopher Y. S. Bull^a, David R. Munday^b, Adrian Jenkins^a

^a *Department of Geography and Environmental Sciences, Northumbria University, Newcastle upon Tyne,
UK.*

^b *British Antarctic Survey, Cambridge, United Kingdom.*

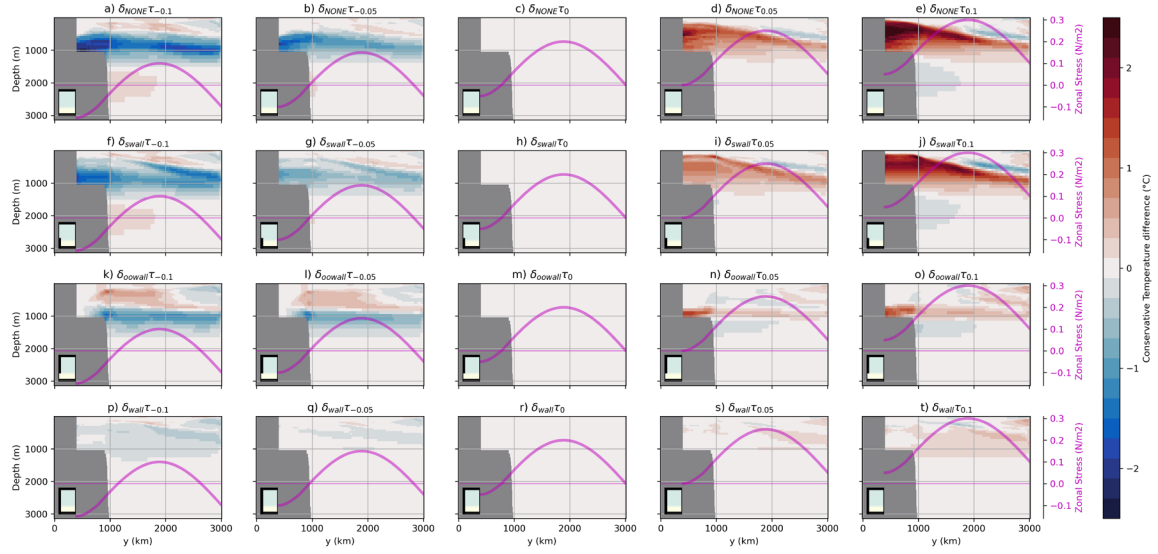


Figure S1. Zonal mean temperature (same data as Figure 6) difference, for all experiments (Table 2) with control removed. Control simulation changes on each row where each row uses the experiment with wind stress offset $c=0$. Middle column then is zero everywhere by definition.

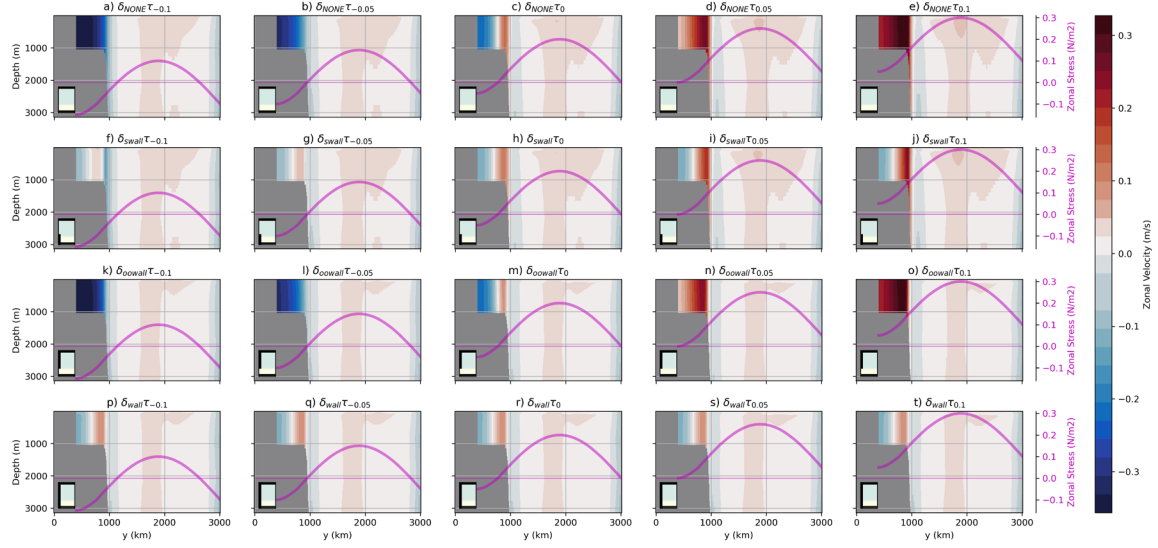


Figure S2. Zonal mean velocity for all experiments (Table 2), with red being eastward and blue westward. Each column has a new wind stress forcing where the middle column is the control wind stress. The magenta line highlights the zonally averaged wind stress. Each row has a different boundary condition, in order: i) fully re-entrant, ii) blocked shelf, iii) blocked deep ocean and iv) fully blocked shelf and deep ocean, respectively. The small glyphs (bottom-left) schematically indicate the geometry under consideration in each panel.

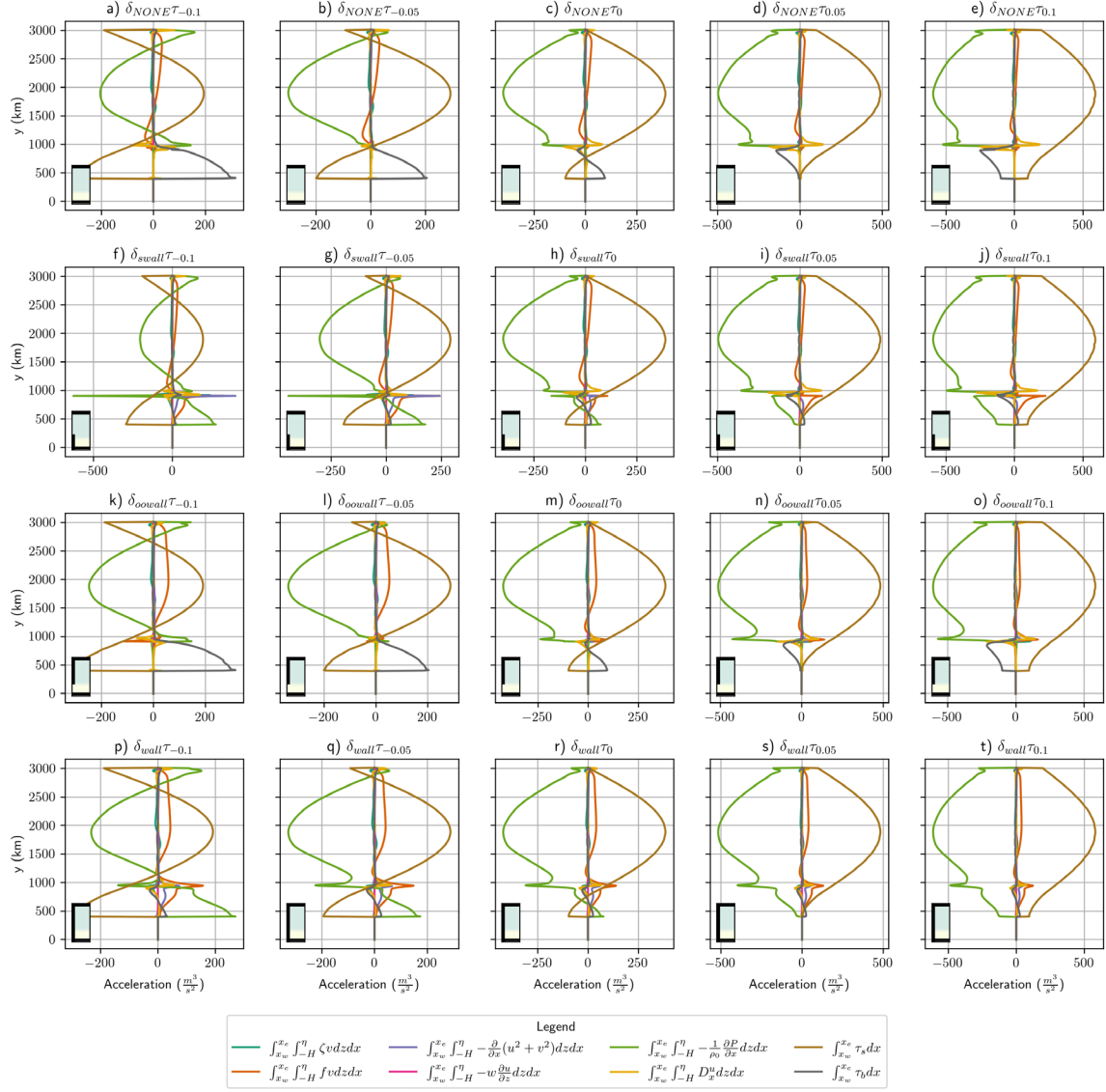


Figure S3. The 10 year time-average vertically and zonally integrated zonal momentum budget. The terms are as described in Section 4.4 and indicated by the legend. Each row has a different boundary condition, in order: i) fully re-entrant, ii) blocked shelf, iii) blocked deep ocean and iv) fully blocked shelf and deep ocean, respectively. The small glyphs (bottom-left) schematically indicate the geometry under consideration in each panel.

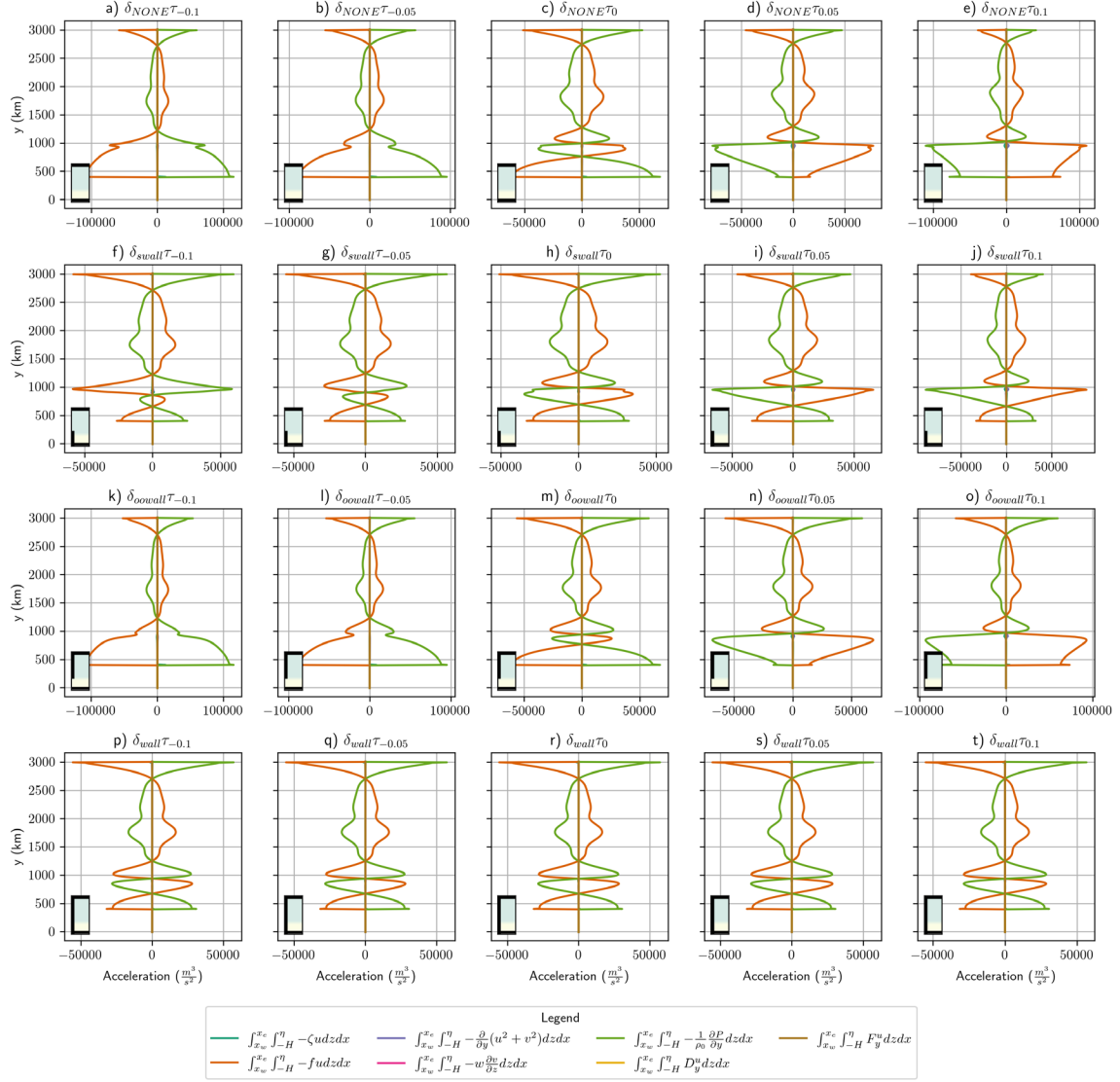


Figure S4. The 10 year time-average vertically and zonally integrated meridional momentum budget. The terms are as described in Section 4.4 and indicated by the legend. Each row has a different boundary condition, in order: i) fully re-entrant, ii) blocked shelf, iii) blocked deep ocean and iv) fully blocked shelf and deep ocean, respectively. The small glyphs (bottom-left) schematically indicate the geometry under consideration in each panel.

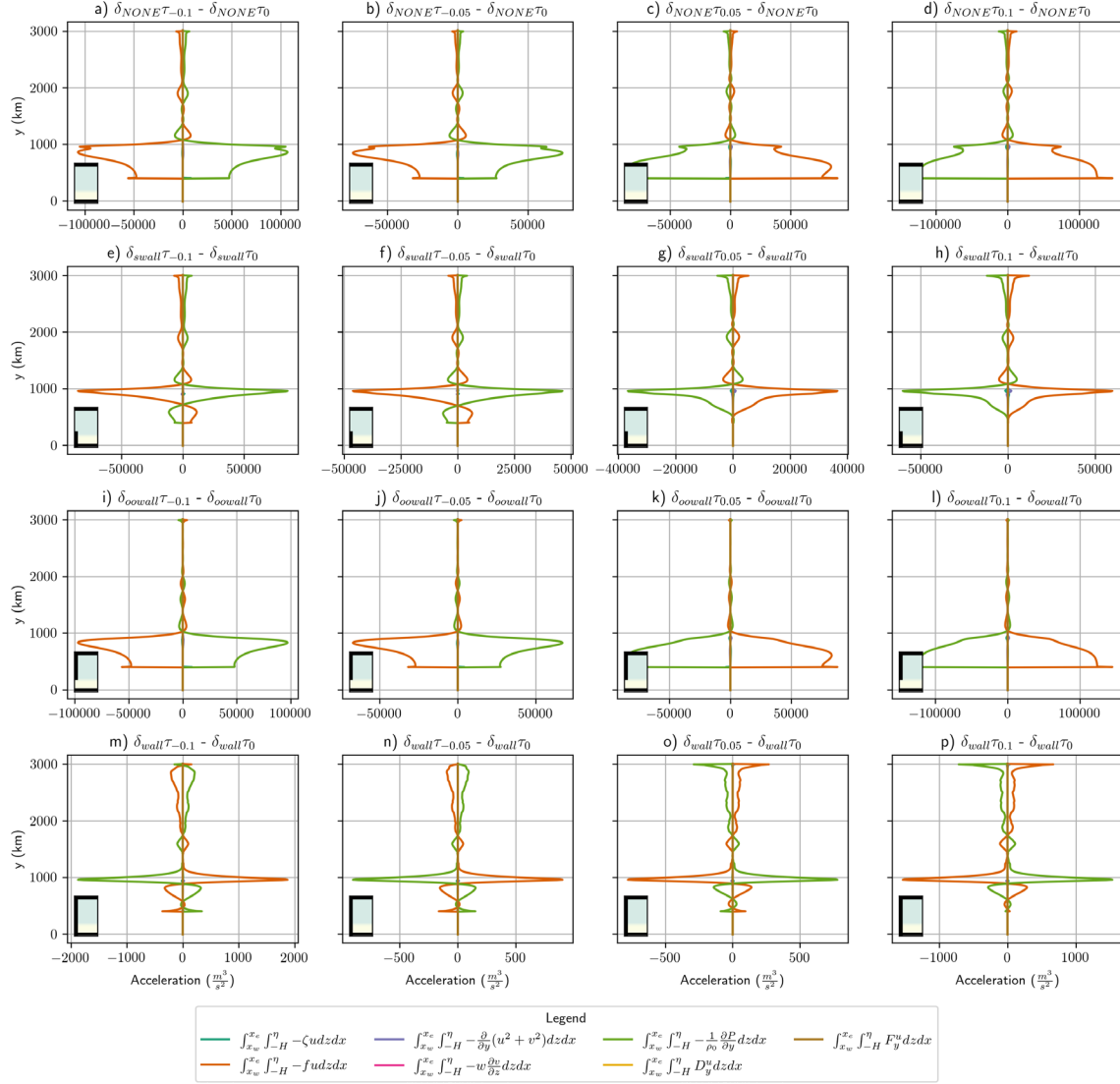


Figure S5. Same as Figure 13 but for the zonally integrated meridional momentum budget (momentum budget anomalies relative to the experiment with the control wind stress). Figure S4 shows the raw values.

Discussion: Figure S2 shows that the zonally averaged currents co-locate with the raw $\int_{x_w}^{x_e} \int_{-H}^{\eta} f u dz dx$ values of Figure S4. Under a change in wind forcing (comparing across the rows), Figure S5 highlights the importance of geostrophy. As the zonal momentum input from the wind changes across the rows in Figure S5, this changes the strength of the zonal flow in the throughflow regimes where a pressure gradient compensates (rows 1-3). In particular, within rows 1-3, columns 1-2 have weaker winds, so the zonal currents decelerate, whereas columns 3-4 have stronger winds, so the zonal currents accelerate. As discussed earlier, there are small changes in the horizontal circulation in a fully gyre regime (row 4) which is why we see relatively small changes in geostrophic balance (note x-axis reduction in scale in row 4). This effect was also discussed in Section 2b and 4c.

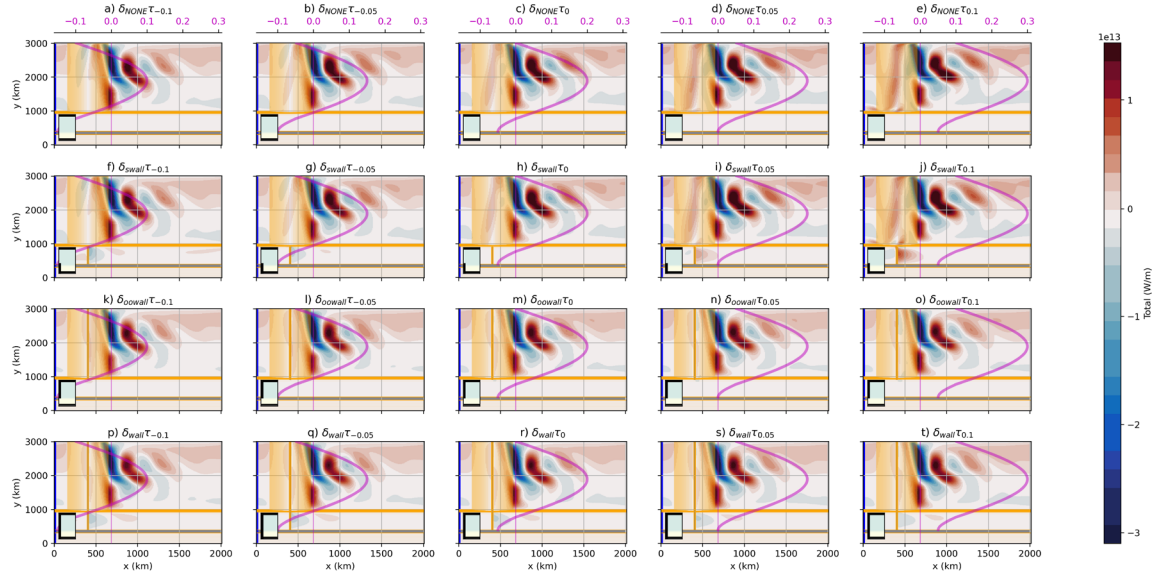


Figure S6. Same panel-experiment layout as Figure 7 but now the total meridional advective heat transport.

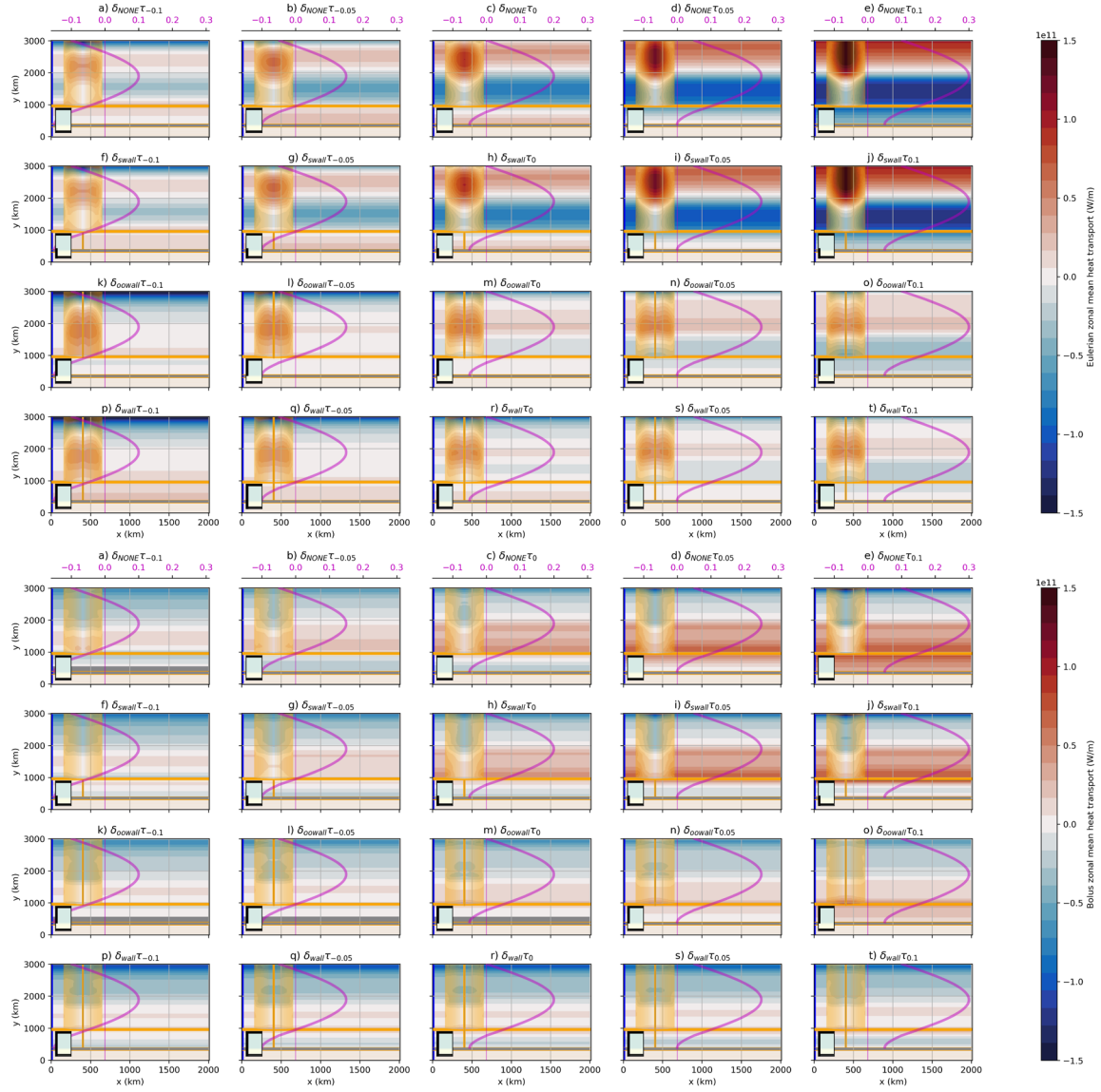


Figure S7. Same panel-experiment layout as Figure 7 but now the Eulerian (top) and Bolus (bottom) meridional *zonal mean* heat transport.

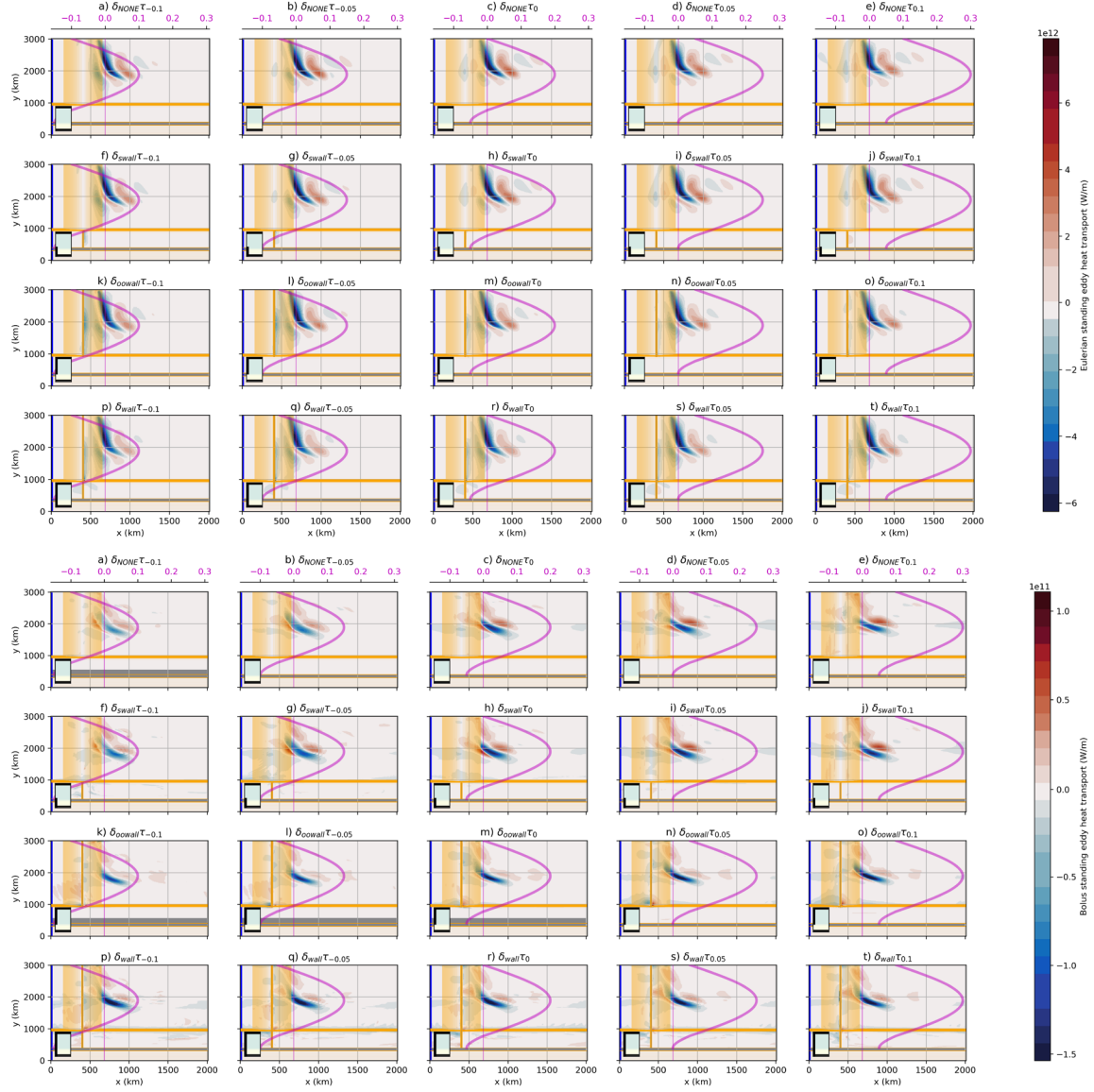


Figure S8. Same panel-experiment layout as Figure 7 but now the Eulerian (top) and Bolus (bottom) meridional *standing eddy* heat transport. Note the change in scale between the top and bottom sets of Figures.

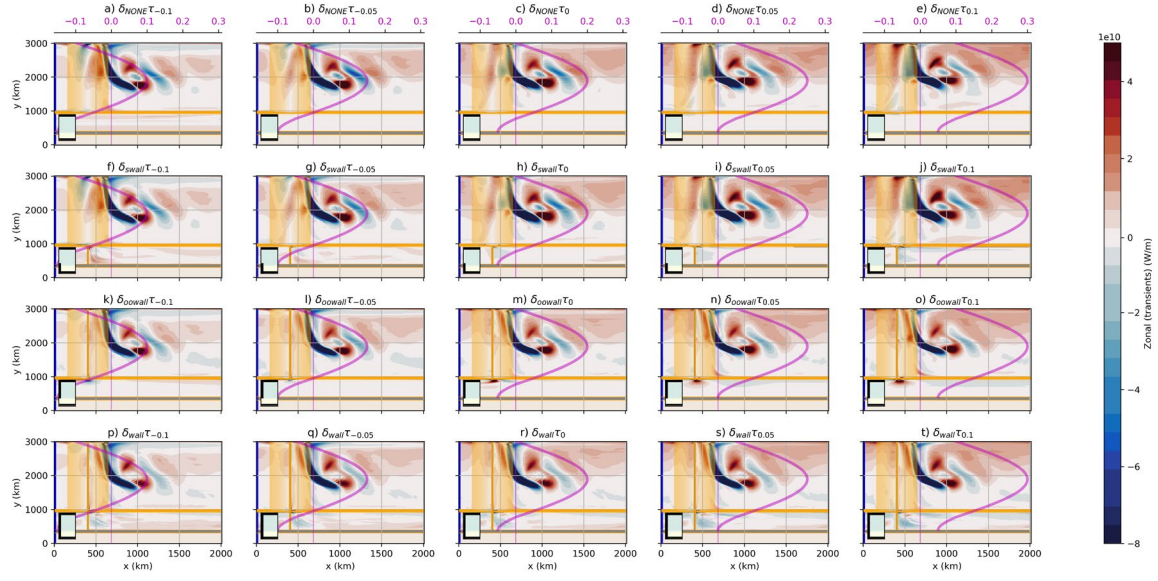


Figure S9. Same panel-experiment layout as Figure 7 but now the Eulerian (top) and Bolus (bottom) meridional *transient* heat transport.